



PONTIFICIA UNIVERSIDAD CATOLICA DE CHILE
FACULTAD DE FISICA
INSTITUTO DE ASTROFISICA

Characteristics of a Galaxy Group at Intermediate Redshift in the SGASJ0033 field

by

Fernanda Gabriela Paz Muñoz Olivares

Thesis submitted to the Faculty of Physics
of Pontificia Universidad Católica de Chile, as one of the requirements
to qualify for the academic Bachelor's degree in Astronomy.

Supervisor : Dr. Felipe Barrientos

Co-Supervisor : Dr. Cédric Ledoux

Committee : Dr. Sebastián López

June, 2023

Santiago, Chile

©2023,Muñoz

Dedicado a Zaphira, Kyra y Taylor Swift

Abstract

We studied the SGASJ0033 field using HST data and a MUSE data cube for photometry and spectroscopy. Our main goal was to analyze a group of galaxies at $z=1.167$ that generated observed arc absorption ($z_{ARC}=2.39$) at the same redshift. We examined various properties of these galaxies, such as their stellar mass, dark matter halo mass, virial radius, and maximum circular velocity. We found that our results were consistent with other similar studies. We also studied the star formation rate using SED fitting and [OII] emission and discovered that differences in the results were related to dust extinction. Furthermore, we confirmed that our galaxies were on the main sequence of the star formation rate, indicating that they were star-forming. We used the Arc-Tomography Technique in bright point sources to study the MgII absorptions caused by the circumgalactic medium, which suggested that more than one galaxy was responsible for the absorption. Finally, we began to investigate the kinematics of the field, observing that stars in the galaxies seemed to show non-aleatory motion and rotation relative to the center of mass, while the gas showed rotation in the same direction. We plan to perform a more detailed kinematic analysis to obtain a more accurate description of the field and determine if any interaction in the group affects the CGM.

Agradecimientos

Quiero agradecerles a todas las personas que estuvieron para mi durante este tiempo. En especial, a mi familia por perderme muchos momentos con ellos por la universidad. A mi madre Marcela y padre Eduardo que siempre confiaron en mis capacidades y apoyaron de forma incodicional. A mi hermano Marcelo por ser mi modelo a seguir. A mi primo Fabyan que siempre ha estado presente para mi. A mis tatas Eugenia y Raúl que son las personas más importantes en mi vida. A mis perritas Zaphira y Kyra que me contuvieron en mis peores momentos. A mis tíos, primos y parientes cercanos.

A todas mis amistades que sin ellos no hubiera sido posible terminar esta carrera. Jose y Tiare, mis amigas más antiguas. Todos los Astrofriends, Amanders, Patineta, Vito, Pancho, Martín, Joacolito, Vitax, Cristi. En especial a las tres primeras, ya que conocerlas fue una de las mejores cosas que me pudo entregar la universidad. A mis amigos físicos, Totoi y Oscar por las largas tardes de estudio y conversaciones profundas. A los SelfLovers, Yeipi y Alfredcillo en donde encontré una amistad muy sincera. A mis amigas del colegio, en especial Jose, Caro y Cata ya que su amistad ha sido de las más reales y duraderas que he tenido en mi vida. A Vicente por acompañarme durante este proceso, leer cada avance y ayudarme a mejorar.

También me gustaría agradecer al profesor Ricardo Sánchez que con su ayuda logré maravillarme por las ciencias. Gracias por las tardes de estudio y gustos compartidos.

Agradezco también al Profesor Felipe Barrientos por sus enseñanzas y confianza que me brindaron muchas oportunidades de las que estaré eternamente agradecida. A Cédric Ledoux que me guió durante todo este proceso y me recibió como parte de su equipo en la ESO.

Por último, agradezco al proyecto FONDECYT 1230231 con el cual se pudo financiar y llevar a cabo este proyecto de investigación.

Contents

Abstract	i
1 Introduction	1
1.1 Galaxy formation and evolution	1
1.1.1 Star-forming galaxies	4
1.2 Circumgalactic Medium	4
1.3 The Gravitational Arc-Tomography Technique: ARCTOMO	5
1.3.1 The MgII-galaxy connection and arc-tomography	7
1.4 Objectives and outline	8
2 Observations and Data	10
2.1 Target selection	10
2.2 HST/WFC3 imaging	12
2.3 VLT/MUSE spectroscopy	12
3 Photometry	14
3.1 Photutils	14
3.1.1 Aperture selection	15
3.1.2 Error estimation	15
3.1.3 Background	16
3.2 DRIZZLE	16
3.3 Measurements and errors	17
3.4 Magnification	18
3.5 Galactic extinction	19

4 Spectroscopy	21
4.1 Moffat model for a star	21
4.2 PyMUSE: optimal extraction	23
4.2.1 Spectra: with and without mask	24
4.3 Corrections: Magnification and Galactic extinction	25
5 Analysis and Results	27
5.1 Emission galaxy properties	27
5.1.1 Halo Mass, Virial Radius and Maximum Circular Velocity . . .	28
5.1.2 Star formation rate	30
5.2 Absorption-Line analysis: MgII	32
5.2.1 Equivalent width	34
5.2.2 Impact parameter	35
5.3 Kinematics	38
5.3.1 Velocity to [OII] and MgII: $z=1.167$	38
6 Conclusion and future work	41
A MUSE: White-Light Image	48
B Photutils apertures	49
C Star modelling	50
D BAGPIPES fitting	52
E Halo-mass estimation	57
F MgII absorption estimation	59

List of Figures

1.1	Madau & Dickinson (2014) Plot	3
1.2	Circumgalactic Medium Cartoon	6
1.3	ARCTOMO Illustration	7
2.1	HST Image: Main Targets	11
2.2	HST Transmission Curves	13
3.1	Magnification Map	18
4.1	Star Spectra	22
4.2	Star Modeling: Moffat Fit	24
4.3	G2 Spectral Data: With and Without Star	25
5.1	Photometry and Spectroscopy Data: OII	28
5.2	BAGPIPES Fit	29
5.3	Main Sequence of the SFR: SFR_{SED} and SFR_{OII}	32
5.4	Dust Extinction	33
5.5	MgII Absorption	34
5.6	Equivalent Width vs Impact Parameter	37
5.7	Velocity and Positions: Absorber Plane	39
5.8	Velocities in X	40
A.1	White Light Image of MUSE	48
B.1	Photutils: Elliptical Apertures	49
C.1	Star Modeling: Star of Field	50

C.2	Recovered Spectra for the Star	51
D.1	BAGPIPES fit: G2	54
D.2	BAGPIPES fit: G3	55
D.3	BAGPIPES fit: G4	55
D.4	BAGPIPES fit: G5	56
D.5	BAGPIPES fit: G6	56
E.1	Halo Mass Estimation	57
F.1	Pyspeckit MgII Fitting	59

List of Tables

3.1	Magnification Factor	19
3.2	Galactic Extinction Factor	19
4.1	Moffat Model Parameters	23
5.1	Galaxy Properties	30
5.2	Star-Formation Rate: SED fitting and [OII]	31
5.3	Equivalent Width and Impact Parameter	35
E.1	Table 6: Moster et al. (2010).	58

Chapter 1

Introduction

1.1 Galaxy formation and evolution

The formation of cosmic structures is influenced by the interaction of two types of matter: baryonic and dark matter. Dark matter interacts primarily through gravity, while baryons interact through electromagnetic forces and collisions that generate photon emission, known as radiative cooling.

Among the most interesting and complex chapters in the formation of cosmic structure is the evolution and origin of galaxies. The observations and study of these structures, formed mainly of dust, gases, and stars, have increased enormously. Multiwave-length imaging surveys with the Hubble (HST), Spitzer, and James Webb (JWST) space telescopes in conjunction with spectroscopic studies at ground-based facilities have led to the discovery of galaxies at redshifts of $z \sim 7\text{-}10$ (Labbé et al., 2023). Despite the growing amount of data collected, it remains challenging to fit and make sense of it, because of the observational difficulty of tracking subpopulations of galaxies undergoing a continuous transformation over cosmic time (Madau & Dickinson, 2014).

The standard cosmological model predicts that primordial density fluctuations grow by gravitational instability driven by cold dark matter (Λ CDM) and without collisions, leading to a "bottom-up" Λ CDM scenario of structure formation (Peebles, 1982). When dark matter clumps and forms halos, baryons collapse toward the center of these halos

when they reach sufficient radiative cooling. This collapse triggers star formation and, eventually, galaxy formation. Large cosmic structures follow hierarchical clustering, with smaller objects collapsing earlier and merging to form larger systems over time. As a result, under certain conditions, galaxies may form galaxy clusters (Blumenthal et al., 1984).

Galaxies are classified into Early Type Galaxies (ETG) and Late Type Galaxies (LTG). These can be further characterized by their star formation rate (SFR) and morphology according to Hubble (1926) where ETGs maintain low SFR, elliptical shapes, reddish colors, and high masses compared to LTGs with disk shapes, high SFRs, and bluish colors (Schawinski et al., 2014).

The properties of some galaxies, such as color and surface mass density, have been observed by the Sloan Digital Sky Survey (SDSS) as bimodal (Madau & Dickinson, 2014). The color-magnitude diagram shows a clear division between LTG in a blue cloud of less massive galaxies and ETG in a red clump of more massive galaxies (Schawinski et al., 2014). The bimodality finds its explanation in the natural evolution of galaxies. As the gas supply is depleted in actively star-forming galaxies, the star formation rate decreases, stellar populations age, and metallicity increases, leading galaxies to move from blue cloud to red clump gradually, without necessarily changing their morphology.

The evolution of galaxies as a function of redshift over cosmic time has been mainly studied by analyzing the star formation rate density (SFRD), representing the number of stars forming per unit of time, volume, and mass in the Universe. The most important results in this area are those of Madau & Dickinson (2014). In Figure 1.1, we show the SFRD versus redshift and lookback time. We note that the SFRD peaked around $z=2$ when the Universe was ~ 3.5 Gyr old and decreased exponentially at $z < 1$, with a characteristic decay time of 3.9 Gyr as the Universe aged. This decrease is observed as the redshift decreases, indicating that the Universe was much more active in the past, with a peak star formation rate approximately nine times greater than the one observed today.

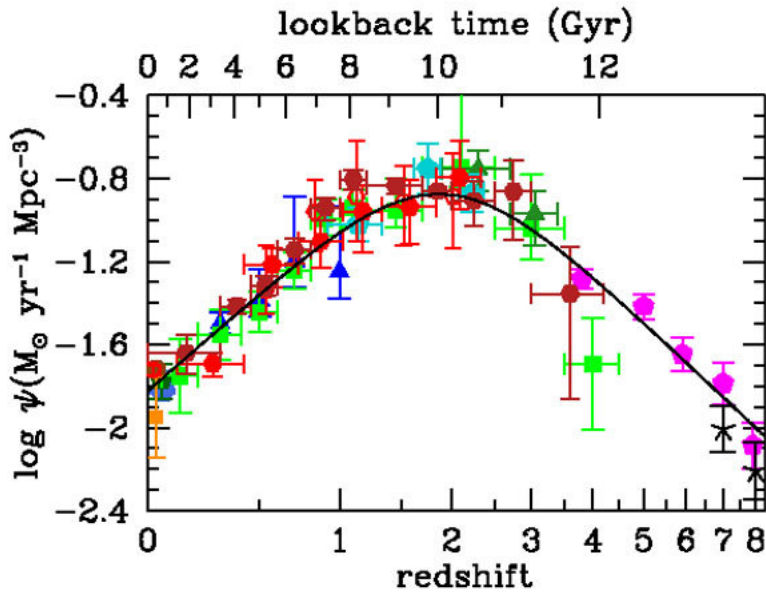


Figure 1.1 Plot extracted from Madau & Dickinson (2014). The figure shows the evolution of the star formation rate density (SFRD) as a function of redshift and lookback time. The horizontal axis shows the redshift of the light emitted by the galaxies as a measure of the distance. The vertical axis shows the SFRD, which indicates the number of stars formed per unit of time, volume, and mass in the Universe. The "lookback time" refers to the interval from when an astronomical object emits light until an observer on Earth detects it.

This information suggests that galaxies have evolved in star formation as the Universe has aged. In the past, galaxies had a star formation rate that increased with time, while today, star formation is lower. This evolution may be related to the availability of cold gas for star formation, as well as to the influence of other processes that also affect this amount of gas, such as energy feedback to the interstellar medium (ISM) and the circumgalactic medium, supernova explosions and supermassive black holes (Madau & Dickinson, 2014).

1.1.1 Star-forming galaxies

We know that blue galaxies have maintained a nearly constant number and stellar mass since $z \sim 1$, while red galaxies have been increasing (Faber et al., 2007). Most actively star-forming galaxies in the redshift range between $0 < z < 2$ have been observed to follow a close correlation, known as the "main sequence", in which star formation rates are related to stellar masses (Wuyts et al., 2014). However, there are starburst galaxies whose star formation rates exceed the main sequence and a growing population of quiescent galaxies that fall below it.

Furthermore, there is a correlation between stellar mass and metallicity (e.g, Salim et al. (2015), Gao et al. (2018), Kashino et al. (2022)). These observed relations between SFR, stellar mass, and metallicity provide insight into the evolution of galaxies through cosmic time.

Emission lines are often used to quantify SFRs. Among the most common ones are H_α . However, as we study galaxies at high redshifts, H_α shifts to infrared wavelengths and becomes inaccessible for some observations. The line of other elements commonly used to measure SFR is [OII] 3728 Å(e.g., Hogg et al. (1998)), but its dependence on the ISM can often introduce uncertainties to the measurements. The intensity of the [OII] line correlates with the amount of ionized gas converted into young stars. By observing the [OII] line, we can determine the current SFR, also known as the instantaneous SFR.

1.2 Circumgalactic Medium

Studying star-forming galaxies is necessary to understand how they acquire gas and convert it into stars within the ISM. However, these processes are not yet well understood (e.g., McKee & Ostriker (2007)). Therefore, several mechanisms have been proposed to describe them.

Galaxies are surrounded by a circumgalactic gaseous medium (CGM) where half of

their baryons are estimated to reside (Werk et al., 2014). This solves the problem of missing baryons since the total amount of baryons accumulated towards the center of galaxies should be much larger than the matter represented by stars. This gas is metal-enriched and in multiple phases, extending up to about 300 kpc (see recent reviews by Tumlinson et al. (2017); Péroux & Howk (2020)). Its multiphase characteristic is composed of cold ionized gas ($T \approx 10^4\text{K} - 10^5\text{K}$) and hot gas ($T \approx 10^6\text{K} - 10^7\text{K}$).

According to those mentioned above, Λ CDM models of galaxy formation, the CGM is a primary environment where baryons cycle in an interaction between pristine cold gas streams from the intergalactic medium and metal-enriched galaxy-scale gaseous flows (e.g., Kereš et al. (2009); Muratov et al. (2015)). Figure 1.2 illustrates this process. Therefore, studying the baryon cycle is key to understanding how star formation in galaxies is regulated through the balance between incoming and outgoing gas and its evolution. However, tracing this cycle remains a challenge mainly because of the low density of the CGM, which is primarily detected in absorption, but also because the traditional technique of quasar absorption lines in galaxies probes only a single narrow pencil beam per galaxy (e.g., Werk et al. (2014); Dutta et al. (2020)).

1.3 The Gravitational Arc-Tomography Technique: ARCTOMO

The gravitational arc tomography technique, introduced by Lopez et al. (2018), uses bright gravitational arcs as background sources to map the full extent of MgII 2796, 2803 Å associated with one or more galaxies along the arcs. These arcs are produced due to gravitational lensing, where light path from a distant object is curved due to gravity, and multiple images of the background sources are produced due to high mass concentrations. Typically, these mass concentrations are associated with clusters of galaxies among the most significant structures in the Universe. This improves the quasar line-of-sight technique's limitation of spatial and statistics-based information to study the CGM, as the multiple images provide several lines of sight to study individual absorbers.

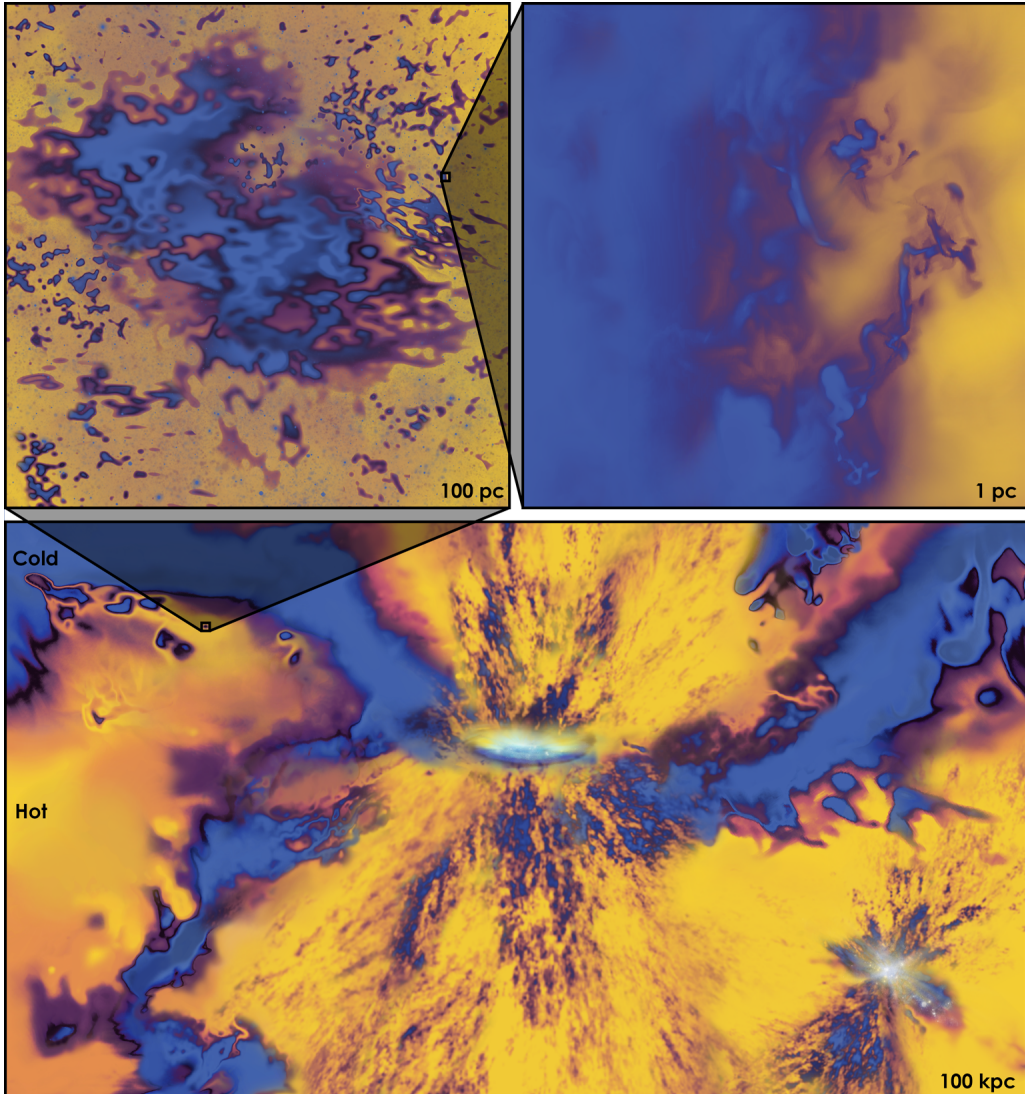


Figure 1.2 Schematic illustration of the CGM from Faucher-Giguere & Oh (2023). The bottom panel shows a central galaxy whose star formation is fueled by a mixture of cold (blue) and hot (yellow) accreting gas and which powers a multiphase galactic wind. The top two panels zoom onto a highly structured cold cloud complex (left) and a turbulent mixing layer (right). In the bottom right the effects of satellite galaxies as additional process to understand the CGM and accurate observational predictions.

The VLT/MUSE observations have been crucial to developing this technique, as they use integral field spectroscopy to study the absorption in the background source produced by intermediate galaxies between the observer and the extended background source. To date, a sample of three strongly lensed arcs in the fields of massive galaxy clusters have been studied by ARCTOMO (2023), developing a set of tools to depro-

ject the lensing effects and to accurately determine the impact parameters from the absorbing gas clouds to the galaxy center. In addition, the technique allows the study of velocity dispersion, equivalent widths, and metallicity for individual galaxies.

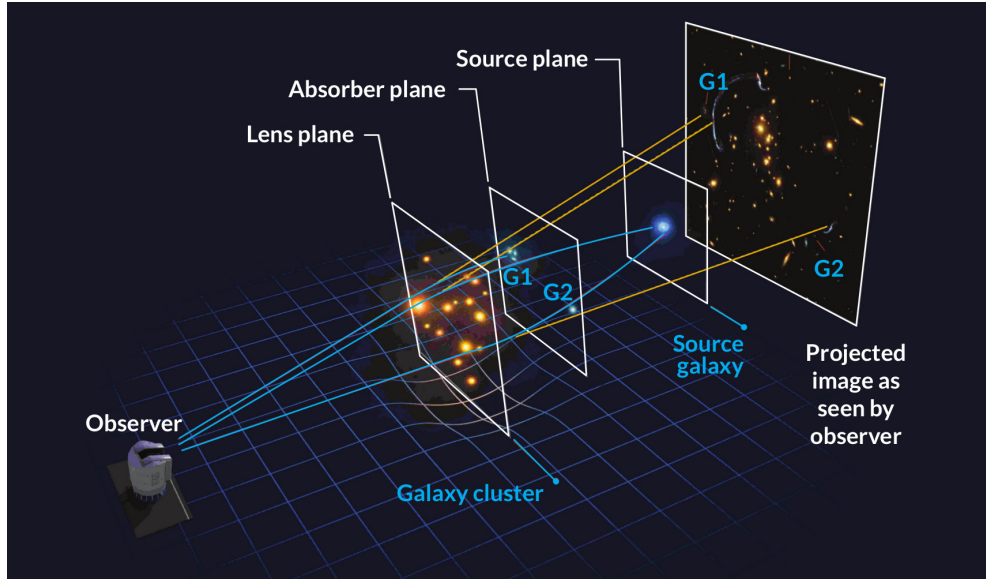


Figure 1.3 Illustration of galaxy cluster RCS 32727-13260 showing in the various planes a gravitational arc (image plane), a lens (lens plane), the intervening absorbers (absorber plane), and the distant source (source plane). Extracted from Lopez et al. (2018).

Figure 1.3 represents the fundamental principles of the technique known as arc-tomography. This technique places a bright-distant light source in the "source plane." This source undergoes significant distortion, deflection, and magnification due to a cluster of galaxies in the "lens plane." As a result, a giant-bright arc is formed and projected onto the "image plane." This arc is used to map the CGM properties of intermediate absorbers. The intermediate galaxies, which generate the absorptions, are placed in the "absorption plane."

1.3.1 The MgII-galaxy connection and arc-tomography

Absorption by the MgII doublet observed in the spectra of bright background quasars provides one of the most sensitive probes of metal-enriched relatively cold gas. It could also trace two critical components of the baryon cycle: galactic-scale

outflow winds (e.g., Bouché et al. (2006)) and cold-mode accretion. However, quasar absorption lines cannot resolve a key aspect of the CGM. The equivalent width (EW), which represents a measure of total absorbed light, is the only quantity we can measure related to the properties of the gas. This is directly related to the gas column density, which indicates the amount of gaseous matter in a specific line of sight from the Earth to a region in space.

MgII has been widely used to study the kinematics and structure of the CGM by several authors (Lopez et al. (2018); Lopez et al. (2020); Péroux & Howk (2020); Nielsen et al. (2013)). It has also been shown to correlate with properties such as the mass of the absorbing galaxy (Ménard & Fukugita, 2012) and its luminosity (Chen et al., 2010).

1.4 Objectives and outline

Since the circumgalactic medium still lacks a precise characterization, we aim to investigate an interesting field, SGAS J003341.5+024217, composed of a galaxy cluster and an arc that exhibits prominent MgII absorption at intermediate redshift. Using this approach, we seek to obtain information on the kinematics and characteristics of the CGM.

In order to achieve this, we focus on a set of galaxies within the field at the redshift at which the absorption of interest is observed and [OII] emission are also shown. By characterizing these galaxies in terms of their stellar masses and SFRs, we can better describe the field and predict which ones may produce the MgII absorption seen in the arc. Furthermore, this characterization will allow comparisons in future studies of the kinematics of the MgII absorption and the [OII] emission that has been detected.

This work is structured as follows. In Chapter 2, we present the observations and target selection. In Chapter 3 and 4, we describe the methodology that includes obtaining photometric and spectroscopy data for subsequent analysis and construction of a model for a central star that affected the measured results. In Chapter 5, we present

the results and discussion on the characterization of the galaxy group and a first visualization of the kinematics of the field. Chapter 6 presents the main conclusions about the galaxy group and its importance in this study.

In the Appendix section, there are several text-referenced figures such as Appendix A, B, and C. In Appendix D, we specify the parameters used for the SED fitting and the results obtained. Finally, the method used to estimate the halo mass is included in Appendix E and the MgII absorption estimates in Appendix F.

In this work, we assume a Flat Λ CDM cosmology, with $\Omega_m = 0.3$, $\Omega_\Lambda = 0.7$ and $H_0 = 70 \text{ km} \text{s}^{-1} \text{ Mpc}^{-1}$.

Chapter 2

Observations and Data

2.1 Target selection

Our target are the main galaxies of the small group of the lensed system SGASJ0033. This system comprises one main gravitational arc and two counter-images of a star-forming galaxy at high redshift, as revealed by the lensing model described by Fischer et al. (2019).

The bright lensed galaxy at $z = 2.39$ was discovered during a survey for giant bright gravitational arcs, which yielded the Magellan Evolution of Galaxies Spectroscopic and Ultraviolet Reference Atlas also known as MegaSaura (Rigby et al., 2018a,b). The lensing galaxy cluster is located at $z = 0.4716$.

We are interested in this field because absorbing gas is observed at the same redshift as the galaxies in the group with emission in OII (3728 Å, 3730 Å). This allows us to examine the characteristics of the galaxies and analyze the kinematics of the group and the CGM.

In Figure 2.1, the six galaxies of the group are recognized as "G". From now on, we will refer to these as a numbering of G.

The selection of these [OII] emission galaxies was realized in a previous spectro-

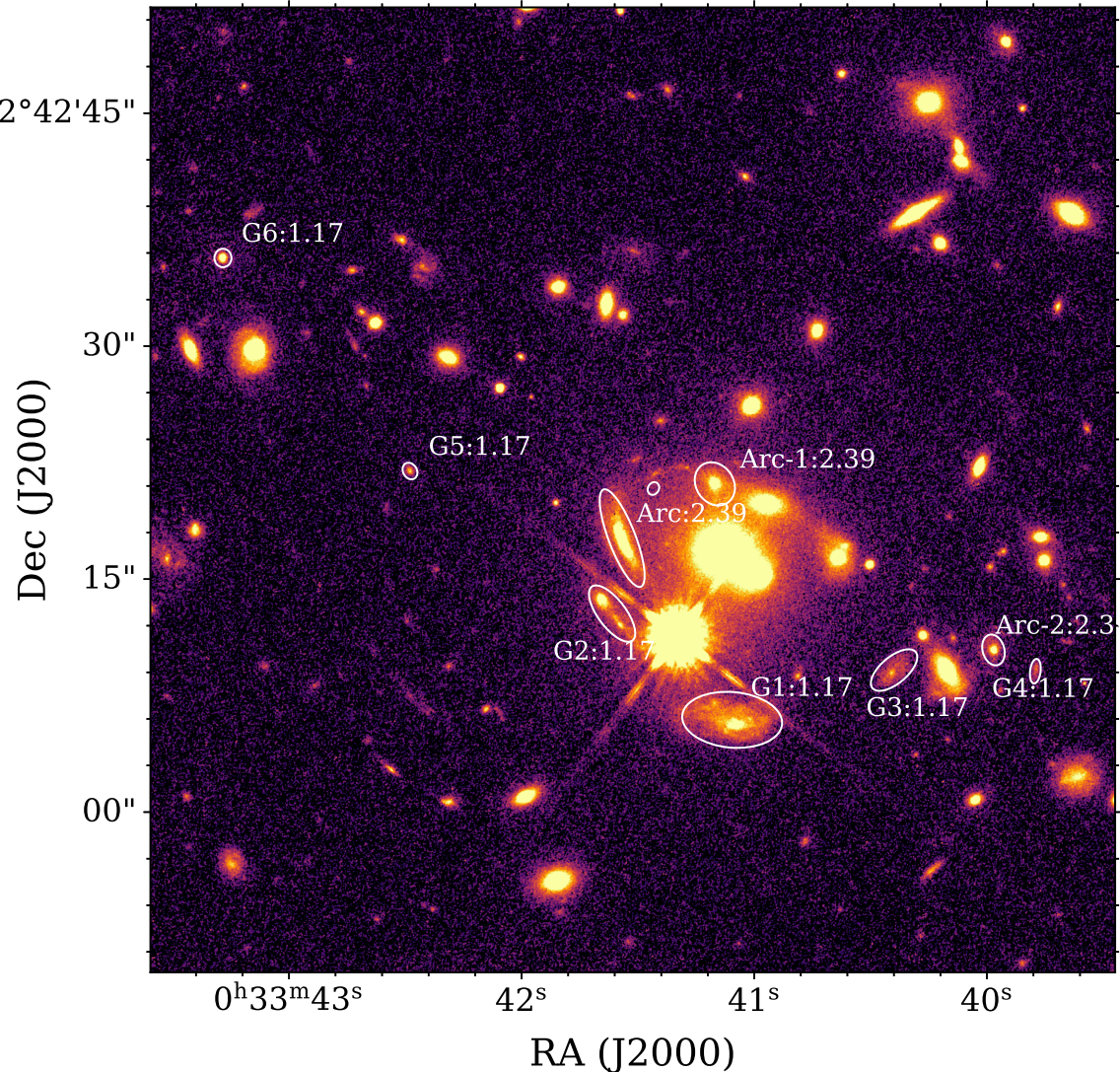


Figure 2.1 Image in the filter F140W obtained from the HST. In white, the main targets within SGASJ0033 and the apertures used for the photometry and spectroscopy process. The galaxies in the group are shown with a "G", and the arc parts with "Arc".

scopic study (Corro-Guerra, private communication) where they obtained the redshift of the field objects and studied their emission and absorption lines. They found that the galaxies are at a redshift of 1.167 and with intense [OII] emission lines, especially for G1 and G2.

The arc and contour images show an absorption of MgII at $z = 1.167$. These images are of the bright lensed galaxy at $z = 2.39$.

2.2 HST/WFC3 imaging

Hubble Space Telescope (HST) data were taken in four different bands for the GO program: GO14170 (PI: Wuyts). The data obtained comprise the F555W, F814W, F105W and F140W bands taken with the Wide Field Camera 3 (WFC3) instrument. All are broadband filters spanning a wide wavelength range, as shown in Figure 2.2.

From left to right, we have F555W, which is in the green-yellow range (~ 555 nm) spanning part of the visible range and then F814W, F105W and F140W spanning part of the near-infrared range centred at ~ 814 nm, ~ 1050 nm and ~ 1400 nm, respectively. These ranges allow us to study star formation in galaxies and the presence of dust, since the near-infrared is the least affected by dust extinction in the interstellar medium.

HST data were reduced using the package `DrizzlePac`. All image data were aligned with the `tweakreg` routine and drizzled to a common pixel size of $0.03''$ with `astrodrizzle` using Gaussian kernels with a drop size of 0.8 (Solimano et al., 2021). Also, the absolute astrometric accuracy of the resulting WCS solution was tested by comparing the centroid position of the foreground stars in the drizzled images with the *Gaia* DR2 catalog (Gaia Collaboration et al., 2018). These results were within $\approx 0.1''$ compared to *Gaia*.

2.3 VLT/MUSE spectroscopy

SGAS observations were carried out at the Very Large Telescope (VLT) using the Multi-Unit Spectroscopic Explorer (MUSE). MUSE is an optical integral-field spectrograph with a Field of View (FoV) of $1' \times 1'$ in its Wide Field mode, a native spaxel (spatial) scale of $\approx 0.2''$, a spectral bin width of 1.25 \AA , and a wavelength range of $4600 \text{ \AA} - 9350 \text{ \AA}$. It uses 24 spectrographs to separate light into its component colors to create

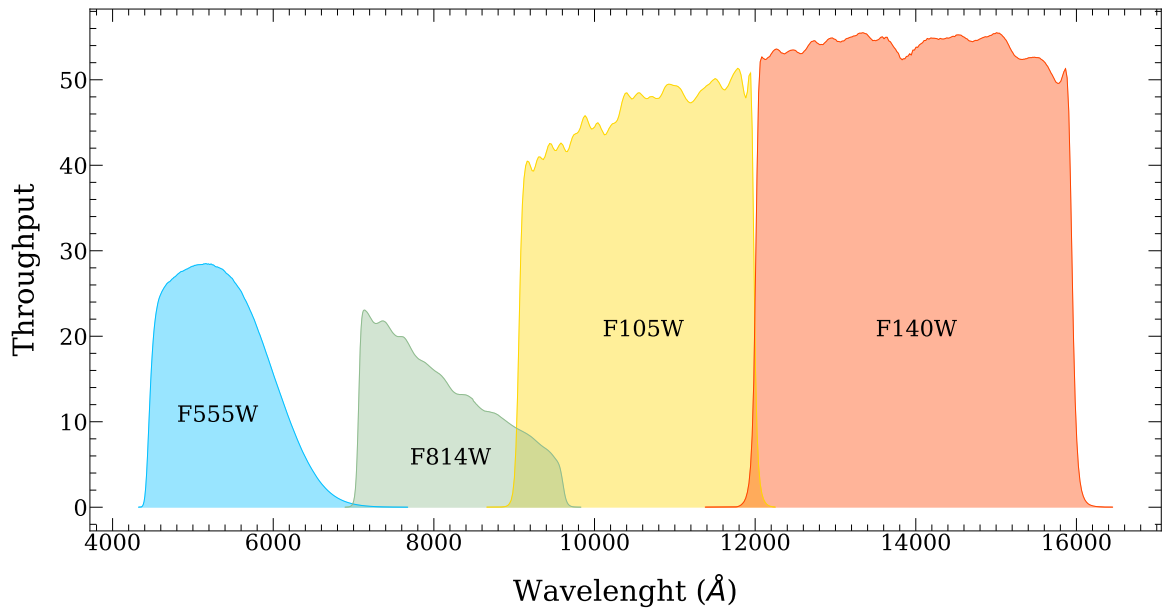


Figure 2.2 HST transmission curves for the different bands available on the data set. F555W (~ 555 nm) in blue, F814W (~ 814 nm) in green, F105W (~ 1050 nm) in yellow and finally F140W (~ 1400 nm) in orange.

both images and spectra of its FoV.

The data were taken during the nights of September 19 and 20, 2017, in natural-seeing mode. Twelve exposures were obtained, each with an integration time of 701 s. The seeing conditions during the observations remained stable around 0.6" FWHM (Full Width Half Maximum). Transparency conditions were mostly photometric, and the target airmass was typically 1.3.

The data reduction was performed using the MUSE pipeline release v2.2 (Weilbacher et al., 2020) running within the ESO Recipe EXecution tool (EsoRex) environment, resulting in the absolute precision of the spectro-photometric calibration being estimated at 0.05 mag. This allowed the cube astrometry to be aligned to match the astrometry of the HST data. More details of the data reduction are described in (Ledoux et al., in prep.). A white light image of MUSE is shown in Figure A.1.

Chapter 3

Photometry

As part of our investigation, we aim to analyze the galaxies of interest by using photometry to measure light in different bands. Thus, we could complement the SED fitting analysis (refer to Chapter 4) and characterize the galaxies regarding their stellar mass and SFR. Furthermore, we intend to compare these results with those obtained by Solimano et al. (2021) for object G1.

This study used HST images in four filters to gather photometry data on specific objects discussed in Section 2.1. There are several ways to count light from astronomical objects in different fields. For our analysis, we used the `Photutils` package of `Astropy` to perform the photometry, and we relied on the `SExtractor` processing since it is a well-known tool for generating photometric catalogues on astronomical images.

3.1 Photutils

`Photutils` serves as a tool for the detection and photometry of astronomical sources. We decided to obtain the fluxes, magnitudes and errors of the sources of interest using the apertures shown in Figure 2.1. In addition, we also recorded the positions of these objects in pixels and spatial coordinates.

3.1.1 Aperture selection

We chose elliptical apertures as these allow us to better fit the shape of galaxies and the arc to get the most out of their flux.

One problem we faced in this field was a star in the region's central zone. Because it is close to two galaxies of interest, we decided to restrict the apertures for the photometry of G1 and G2 to minimize the amount of flux that the star can introduce to the photometry measurement.

3.1.2 Error estimation

`Photutils` does not directly estimate the errors associated with the fluxes measured by photometry. Therefore, we had to perform this process on our own. We decided to follow the same idea of the `SExtractor` software and estimate the errors from the flux measured at each aperture as follows,

$$\text{FLUXERR} = \sqrt{\sum_{i \in A} (\sigma_i^2 + \frac{p_i}{g_i})} \quad (3.1)$$

Where A is the set of pixels defining the photometric aperture, and σ_i , p_i and g_i are, respectively, the noise standard deviation estimated from the local background, the pixel value in the measurement image subtracted from the background and g_i the effective detector gain (Holwerda, 2017).

The magnitudes and their errors are also estimated from the flux as follows:

$$\begin{aligned} \text{MAG} &= \begin{cases} \text{MAG_ZEROPOINT} - 2.5 \log_{10} \text{FLUX} & \text{if FLUX} > 0 \\ 99.0 & \text{otherwise} \end{cases} \\ \text{MAGERR} &= \begin{cases} \frac{2.5}{\ln 10} (\text{FLUXERR}/\text{FLUX}) & \text{if FLUX} > 0 \\ 99.0 & \text{otherwise} \end{cases} \end{aligned} \quad (3.2)$$

Where the fluxes are in counts (ADUs).

3.1.3 Background

For background measurement in each aperture, we used a function delivered by `Photutils` that uses the procedure described by `SExtractor` for a **crowded case**: $2.5 \times \text{median} - 1.5 \times \text{mean}$, with a value of 3σ for the *sigma clipping* process in the background estimation. The values were calculated in annular apertures around each source as seen in Figure B.1.

3.2 DRIZZLE

HST images use a processing method called `DRIZZLE` to combine multiple subsampled images into a single high-resolution image (see Fruchter & Hook (2002)). This method preserves photometry and resolution without sacrificing the final signal-to-noise ratio and reduces distortion (Casertano et al., 2000). It does this by first aligning the input images to a common reference frame, correcting for any geometric distortion that may be present in the images. Then, it divides each input pixel into a grid of smaller sub-pixels and assigns a weight to each sub-pixel based on the statistical significance of the data in that region. The overlapping subpixels of adjacent input pixels reconstruct missing information in regions where data are undersampled or missing due to cosmic rays or detector defects. Finally, it combines the weighted sub-pixels from all input images to produce a final high-resolution image.

Despite its effectiveness in combining images, it has been found that pure photometric errors will be incorrect if using the `DRIZZLE` method (Gal, 2023). This is because the output pixels in the `DRIZZLE` images are not independent. Hence, the noise in individual pixels is not the same as for the input images and does not scale as it would for respective pixels. In particular, when we estimate noise over an area, the correlation between pixels makes the total noise larger than the quadratic combination of the noise in individual pixels (Casertano et al., 2000).

The correction factor is proposed by Gal (2023) and is expressed as:

$$\sqrt{F_A} = \begin{cases} (s/p)(1 - (s/3p)) & \text{if } s < p \\ 1 - p/(3s) & \text{if } s > p \end{cases} \quad (3.3)$$

p is the pixel fraction and s is the pixel scale. In our case, $p = 0.5$ and $s = 0.03''$.

3.3 Measurements and errors

Based on the above, we measured the flux in the image with the local background already subtracted at each aperture with `Photutils`.

Then, the error in the photometry was calculated using the equation 3.1. For p_i and σ_i , we measured over each pixel within the aperture in the image minus the background and over a background image created from `SExtractor`, respectively. Considering that the images in the different filters are in units of e^-/s , for p_i , we multiply each by the exposure time and the number of images given by the `DRIZZLE` processing. This allows us to keep the units described by Holwerda (2017). The gain g_i was obtained from the `header` of the images.

After calculating the error values, we can reverse the process by dividing by the exposure time and number of images. This will convert the values to their original units and make them comparable to the initial fluxes. In addition, we obtain the correction factor $\sqrt{F_A}$ for the effects of `DRIZZLE` according to the equation 3.3. Then, we obtain the corrected error:

$$\text{FLUX_ERR_CORRECT} = \frac{\text{FLUX_ERR}}{\sqrt{F_A}} \quad (3.4)$$

$$\text{MAG_ERR_CORRECT} = \frac{\text{FLUX_ERR_CORRECT}}{\sqrt{\text{FLUX}}} \cdot \frac{2.5}{\ln(10)} \quad (3.5)$$

For the flux and magnitude, respectively.

3.4 Magnification

Since we are in front of a cluster that produces a lensing effect that magnifies the objects in the sector, it was necessary to correct the magnification effects on the fluxes. Figure 3.1 shows the magnification map for the study area provided by Ledoux, C. This map was created from observations and gravitational lensing models.

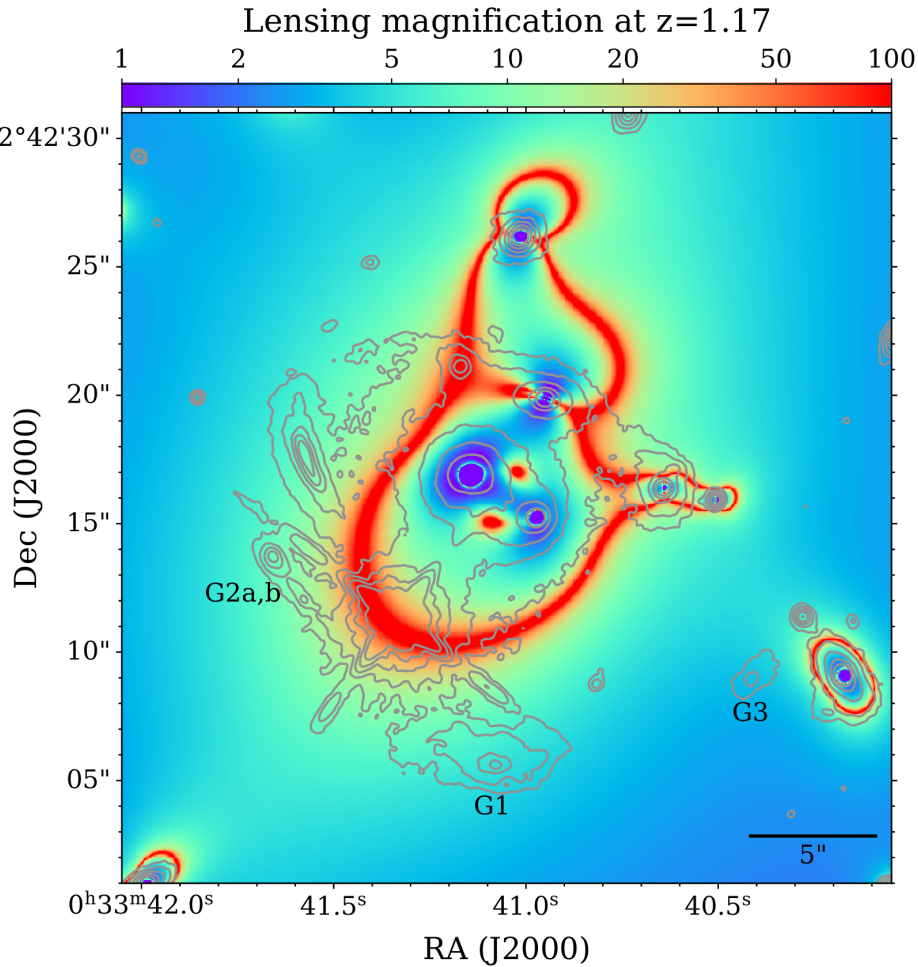


Figure 3.1 Magnification lensed in the absorption plane at a redshift of $z=1.17$. The color bar indicates higher magnification values are associated with red, while less magnified regions are in blue. Ledoux, C. provided the magnification map used.

A magnification value within each aperture was obtained using the median value. The median will represent a more robust result than the average of the data. This is chosen since we are looking for a magnification value that represents the central part

Table 3.1. Magnification Factor

Object	Magnification Factor
G1	5.6 ± 2.3
G2	10.5 ± 5.0
G3	3.7 ± 2.7
G4	2.1 ± 0.5
G5	2.1 ± 0.4
G6	1.5 ± 0.3

Note: The magnification values was calculated from the median of the data in the previously defined apertures for each source within the magnification map. The uncertainty is the standard deviation σ calculated within the same aperture.

Table 3.2. Galactic Extinction Factor

Filter	$\lambda_{eff}(\mu\text{m})$	Band Extinction (mag)
F555W	0.54	0.059
F814W	0.80	0.032
F105W	1.04	0.020
F140W	1.37	0.013

Note: Galactic extinctions for the WFC3 filters. The values for λ_{eff} and the extinction band are according to Schlafly & Finkbeiner (2011).

of the galaxy rather than the edges of the apertures. The result is an approximation of the real magnification. The values for each galaxy are in Table 3.1.

The magnification factors were used for each galaxy to divide the calculated fluxes.

3.5 Galactic extinction

In addition to the magnification effect, it was necessary to correct for galactic extinction. The extinction band for each filter was obtained from Schlafly & Finkbeiner (2011), and the corresponding values are shown in Table 3.2.

Assuming that our extinction correction factor is given by A and is in units of

magnitudes, we see that it will be equivalent to:

$$m_{corr} = m_{obs} - A \quad (3.6)$$

Where m_{corr} and m_{obs} are the extinction-corrected apparent magnitude and the observed apparent magnitude, respectively. Furthermore, from the difference of apparent magnitudes, we have that,

$$m_1 - m_2 = -2.5 \log_{10} \left(\frac{F_1}{F_2} \right) \quad (3.7)$$

Developing these expressions, we can find a relation between the corrected flux (F_1), observed flux (F_2) and the extinction correction (A) in units of flux. This relation is shown in the equation 3.8 and is used to correct the photometric fluxes.

$$F_{corr} = F_{obs} \cdot 10^{0.4A} \quad (3.8)$$

In Chapter 5, we will analyze the characteristics of the objects of interest using the code **BAGPIPES**, based on the results obtained. The next chapter will cover obtaining the spectra of these objects and how we addressed the issue of the star in the field in the MUSE data.

Chapter 4

Spectroscopy

We studied the spectra of the objects we were interested in to look for absorption and emission lines. This will help us analyze the characteristics and kinematics of the galaxies in that particular region. Specifically, we focused on [OII] emission and MgII absorption lines.

4.1 Moffat model for a star

In Chapter 3, we mentioned the problem of the bright star near G1 and G2 galaxies. Its spectrum is shown in Figure 4.1. Based on our analysis, it can be identified as a K-type star due to the faint presence of Balmer lines H_α and H_β , as well as other absorption lines indicated by Mg and Na. Additionally, there are observed sky lines towards the red end of the spectra.

When obtaining photometry, we decided not to remove the flux contribution from the star for the HST data. When working with MUSE data, the sources are more spread out than HST data. As a solution, we chose to model the star to obtain a cube that excludes the star and provides improved results for G2. Moffat is known to describe well the light distribution of a star (Moffat, 1969). The model was made using the `MoffatModel2` function from the `MPDAF` package.

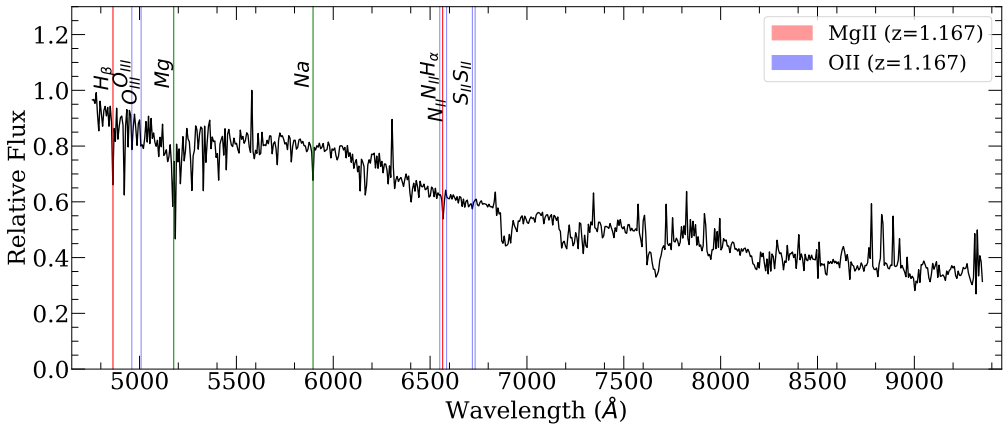


Figure 4.1 Spectra of the field star classified as type K. The regions of interest for MgII and OII at redshift 1.167 are shown in red and blue. In red, the Balmer lines H_α y H_β . In blue, OIII, NII and SII. In green Mg and Na.

We made a 1.5" mask in the central part of the star because the model does not fit correctly in that area. Since we are interested in extending the model to the G1 and G2 galaxy regions, it was enough to model the "wings" of the star. We used a `size` of 5", `fwhmdeg` of 3 and `betadeg` of 2 for the model estimation.

On this result, a model covering 20" was recalculated and extended to the rest of the cube. This was done with the objective that the first model was restricted to cover the star with no contribution from light from nearby galaxies and then extend spatially.

For different stars in the field, we performed a model with a 5" size to test the method. These stars are less bright than the central star and are far from the cluster. The results of the full width at half maximum (FWHM) and Beta parameters for three of these stars are shown in Table 4.1. For more details of these parameters, see MPDAF (2023).

In Figure C.1, we show one of the stars with the fit performed and its residuals. We can check the method's effectiveness from the residuals since no flux is overestimated or added to the image's background.

Table 4.1. Moffat Model Parameters

Star	FWHM	Beta
0-Mask	0.963	2.576
0	0.676	2.961
1	0.837	2.092
2	0.856	2.278
3	0.895	2.064

Note: Parameters values of the moffat model realized for a size of 5 arcsecs. The center star is 0 for the fit with and without mask. The three stars in the field are designated as 1, 2 and 3. Both parameters are expressed in arcsec.

We observed that the model's parameters for the central star change with or without a mask. In Bacon et al. (2023), they found that the FWHM for this star is $0.7''$, and our results with a mask align with this value, which we have selected as the correct one.

In Figure 4.2, we see that the model fits the "wings" of the original data. At 180 pix value, we estimate G2, the nearest galaxy, and we can see that the extended model fits correctly to the star profile.

The final data cube with the model subtracted from the star was used to obtain spectra.

4.2 PyMUSE: optimal extraction

The PyMUSE package (Pessa et al., 2018) is optimized to extract 1-D spectra from arbitrary spatial regions within the cube. We use the 'White Weighted Mean' (wwm) extraction mode, based on the weighted mean where the weights are obtained from the white-light image. It is smoothed using a Gaussian filter with $\sigma = n_{pix}$. The extraction apertures are the same as in photometry but considering a factor of $seeing = FWHM = 0.6''$ as follows.

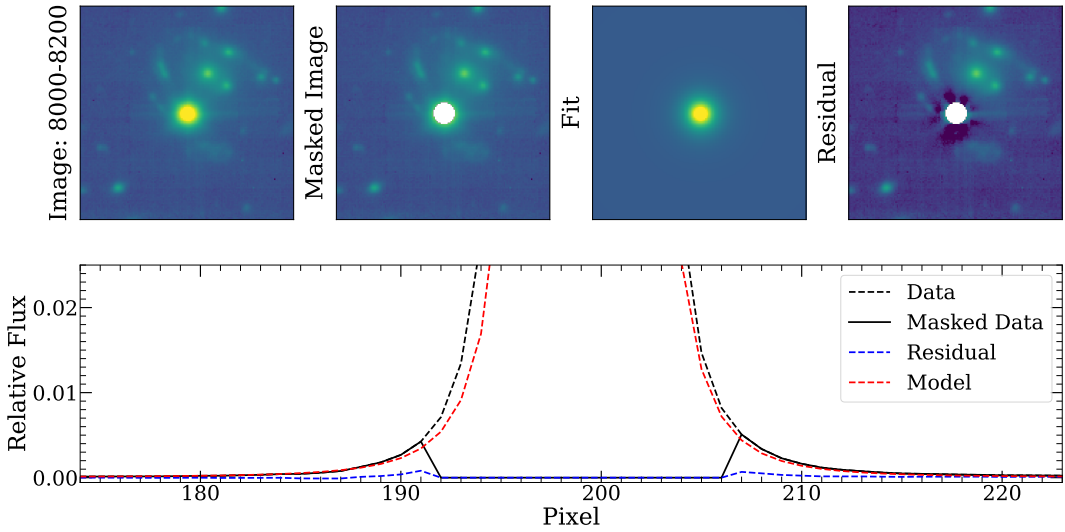


Figure 4.2 At the top, the image in the wavelength range at $z=1.167$ covers the [OII] emission lines, the mask, the fit and the residuals. At the bottom, a horizontal projection of the images. We see the fit in red and the residuals in blue.

$$v'_i = \sqrt{v_i^2 + FWHM^2} \quad (4.1)$$

Where v_i represents the semi-major axis a or the semi-minor axis b of the ellipse definition.

4.2.1 Spectra: with and without mask

Figure 4.3 shows the comparison between the spectra for G2 obtained in the original cube versus that obtained in the cube without the star.

We note a more significant difference in the spectrum towards the blue when comparing data with and without a star. Upon examining the star's spectra (refer to Figure 4.1), we concluded that the star caused the flux contribution towards the blue and has been mostly eliminated. To verify this, we subtracted the Data and Mask-Data and recovered the star's spectra (see Figure C.2). We achieved flux recovery for [OII] in the

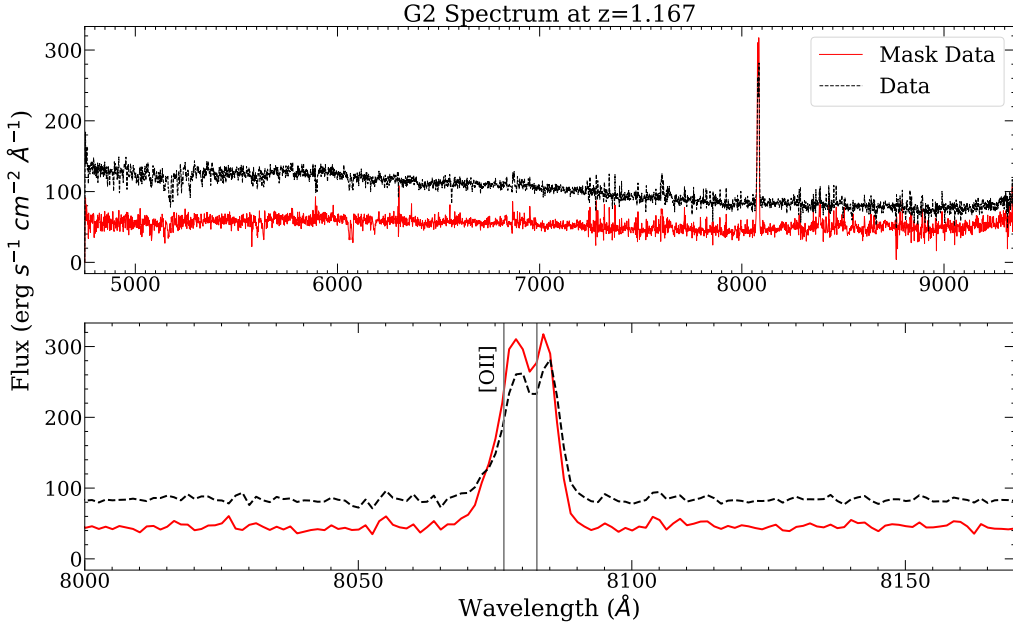


Figure 4.3 At the top, the spectra obtained with PyMUSE on the original cube (Data) and the cube without star (Mask Data) for G2. The wavelength range is at $z=1.167$. At the bottom, a zoom of the [OII] emission.

area of interest, which helped us improve our results in characterizing G2.

4.3 Corrections: Magnification and Galactic extinction

Like the photometric data, the spectra were corrected for magnification and galactic extinction. For magnification, the spectra were divided by the factors described in Table 3.1. For the galactic extinction, we utilized the `extinction` package in the `ccm89` mode (Cardelli et al., 1989). This package provides a range of extinction values for all wavelengths.

It is known that the general shape of the extinction curve in the ultraviolet (UV) is well parameterized by R_V described as:

$$R_V = \frac{A_V}{E(B-V)} \quad (4.2)$$

Where A_V is the total extinction in the visible band and $E(B-V) = A_B - A_V$, the difference between the extinction in blue wavelengths and the visible band. We use $A_V = 0.058$ and $A_B = 0.076$ obtained from Schlafly & Finkbeiner (2011). It is known that the typical value of R_V is 3.1 (Schultz & Wiemer, 1975). Using the values proposed by Schlafly & Finkbeiner (2011), we found a R_V of 3.2.

The spectrum was corrected using the equation 3.8 with the calculated extinction values.

Chapter 5

Analysis and Results

5.1 Emission galaxy properties

We used the BAGPIPES software (Carnall et al., 2018) to estimate the stellar mass (M_*) of galaxies from both HST photometry and MUSE continuum spectra. Figure 5.1 shows the photometry on the spectra with recognized [OII]. The stellar population models used by BAGPIPES are the 2016 versions of those of Bruzual & Charlot (2003) assuming the stellar initial mass function (IMF) of Kroupa & Boily (2002). The star formation histories were modeled as double power laws. For more details on the parameters we fit and priors, review Appendix A. Figure 5.2 shows the fit made by BAGPIPES.

The photometry fits the spectra and to the SED fit. Consequently, the results will be consistent.

Table 5.1 shows the stellar masses we obtained. G1 shows the highest stellar mass of $\approx 10^{11.01} M_\odot$, followed by G3 $\approx 10^{10.56} M_\odot$ and G6 $\approx 10^{10.22} M_\odot$. For G1, we find that our result differs by about 0.46 dex with that proposed by Solimano et al. (2021) given by $M_* = 10^{10.55^{+0.27}_{-0.24}}$. One possibility to explain this discrepancy is the method used to calculate stellar masses. In Solimano et al. (2021), they used MAGPHYS and two more ACA filters. In addition, we used smaller apertures to minimize contributions from the central star; however, given the large systematic errors present in both derivations, the true value may lie between the two values.

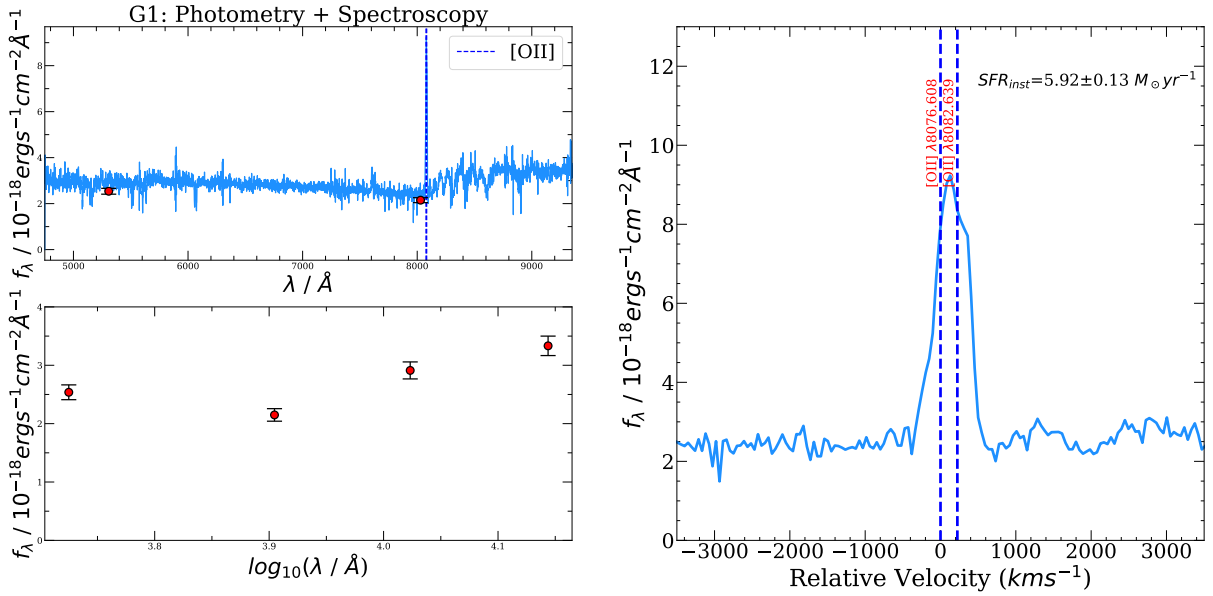


Figure 5.1 The MUSE spectrum for G1 is shown on the top left, with the photometry overlaid with recognized [OII]. The bottom section displays the HST photometry in the four filters. On the right side, the [OII] emission line for G1, with the relative velocity indicated for the first line of the [OII] doublet. By observing the intensity of the [OII] line, we can determine the instantaneous SFR.

5.1.1 Halo Mass, Virial Radius and Maximum Circular Velocity

Stellar masses imply a dark matter halo mass for each galaxy. We rely on the "Stellar-to-halo Mass Relation" of Moster et al. (2010) to obtain the halo masses (M_h). For more details, review Appendix D.

The virial radius is the radius within which the mass density equals Δ times the critical density of the Universe $\rho_c(z)$, enclosing a virialized halo of mass. Using the mass of the halo, this is expressed as $R_\Delta = [3M_h/(4\pi\Delta\rho_c(z))]^{1/3}$. It is commonly used $\Delta = 200$, which implies a radius where the mass density of the halo is equal to 200 times the critical density of the Universe. We will consider $R_{200} = R_{vir} = [3M_h/(4\pi 200 \rho_c(z))]^{1/3}$,

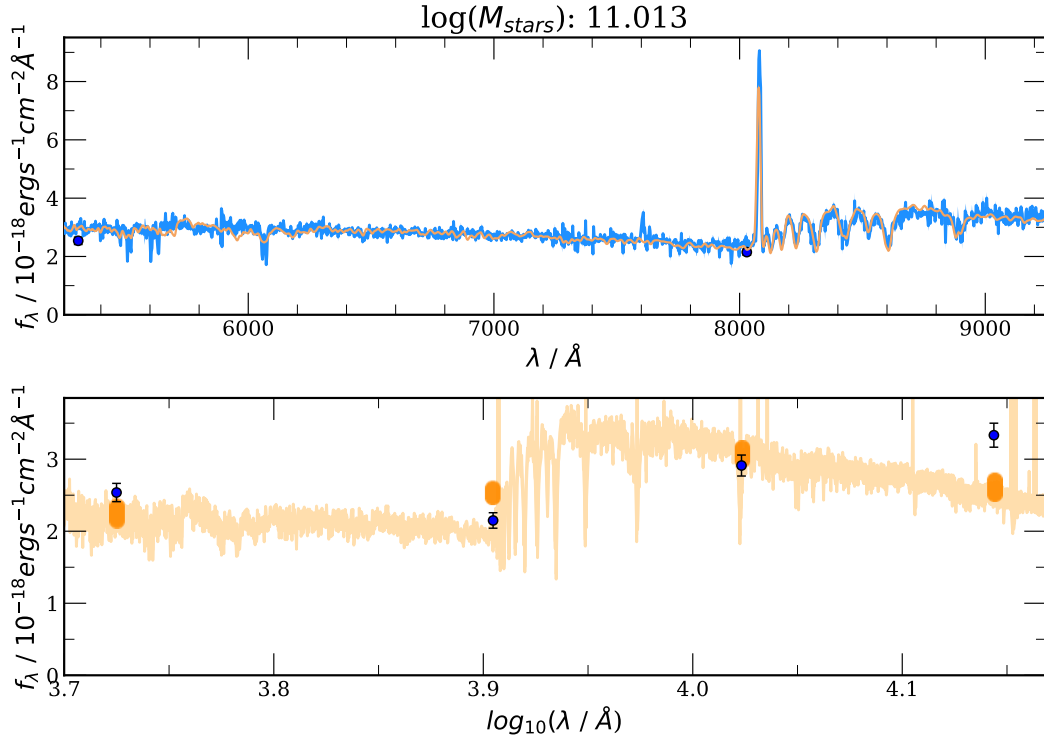


Figure 5.2 At the top, the model fit performed by BAGPIPES in orange, and the MUSE spectra and HST photometry in line and blue dots, respectively. Below, the output for photometry in orange and HST photometry in blue.

as the size of the DM halo of a galaxy, as well as the limit of the CGM of a galaxy, which encloses a total mass M_{200} . According to Mo et al. (1998) we have that

$$\rho_c = (3H^2)/(8\pi G).$$

The maximum circular velocity is the highest orbital velocity experienced by a star or gas cloud in the galactic disk. We estimated this velocity as $v_{max} = [10M_hGH(z)]^{1/3}$, where G is the gravitational constant and H(z) is the Hubble parameter at redshift z.

The results, as for the stellar masses, are shown in Table 5.1. The errors were estimated by propagating the errors from the stellar masses.

The galaxies G1, G3, and G6 show the highest values for M_h , R_{vir} , and v_{max} . This

Table 5.1. Galaxy Properties

Object	$\log(M_*)(M_\odot)$	$\log(M_h)(M_\odot)$	$R_{vir}(kpc)$	$v_{max}(km/s)$
G1	11.01 ± 0.08	12.93 ± 0.16	271 ± 33	368 ± 32
G2	10.14 ± 0.06	11.96 ± 0.03	129 ± 3.0	175 ± 4
G3	10.56 ± 0.12	12.26 ± 0.12	162 ± 14	220 ± 15
G4	9.56 ± 0.18	11.69 ± 0.08	105 ± 6.0	142 ± 7
G5	9.44 ± 0.16	11.64 ± 0.07	101 ± 5.0	137 ± 6
G6	10.22 ± 0.22	12.00 ± 0.13	134 ± 13	181 ± 14

Note: The uncertainty for M_* represents 2σ of the posterior distribution, while the rest of the uncertainties were estimated by propagating these errors.

observation is consistent since these three parameters are directly related to the stellar mass and are, therefore, representative of it. Moreover, when comparing our results with similar investigations in related fields (see Tejos et al. (2021)), where the same study was carried out in an isolated galaxy, we find that our values are within the same order of magnitude as those obtained in that investigation for G1 in SGAS J1226+2152.

5.1.2 Star formation rate

We used the MUSE spectra and estimated the instantaneous SFR from the doublet of [OII]. With `pyspeckit` (Ginsburg et al., 2022), we fit the spectra continuum and Gaussian profiles to the emission lines and measure the total integrated flux $f[\text{OII}]$ (corrected for galactic extinction and magnification). Then from Kennicutt (1992), we convert from $f[\text{OII}]$ to SFR. The general relation is given for measurements in $H(\alpha)$, but we will use the luminosity of [OII] as follows.

$$SFR(M_\odot \text{yr}^{-1}) = 2.0 \times 10^{-41} L[\text{OII}] \quad (5.1)$$

This result was further corrected by the geometric factor $4\pi l_{dist}^2$ to account for the geometry of the emission source. The errors were propagated from the amplitude and standard deviation of the Gaussian fit. Furthermore, a 5% error derived from the photometric calibration based on the observations was considered. Since these errors are

Table 5.2. Star-Formation Rate: SED fitting and [OII]

Object	$SFR_{SED}(M_{\odot}yr^{-1})$	$f[OII](10^{-18}ergs^{-1}cm^{-2})$	$SFR_{inst}(M_{\odot}yr^{-1})$
G1	63.68 ± 0.052	210 ± 4.60	5.92 ± 0.32
G2	4.864 ± 0.065	139 ± 1.20	2.09 ± 0.10
G3	13.43 ± 0.070	21.1 ± 0.87	0.90 ± 0.06
G4	1.374 ± 0.546	7.40 ± 0.49	0.56 ± 0.05
G5	17.66 ± 0.178	13.8 ± 0.23	1.04 ± 0.06
G6	1.250 ± 1.382	7.81 ± 5.30	0.82 ± 0.56

independent, the root of quadratic sums was calculated as the final error. Systematic errors were not taken into account. The integrated flux ($f[OII]$) and results for the SFR are given in Table 5.2.

From the results of **BAGPIPES**, we derived an SFR from SED fitting. The results are also in Table 5.2.

The calculated SFRs are compared in Figure 5.3. The maximum difference is found in G5 at 1.23 dex. This difference can be attributed to the fact that in the SFR calculations based on [OII], the internal extinction of the galaxy due to dust was not considered. Using the values provided by **BAGPIPES** for the dust extinction, we have estimated a first-order relation to the difference between the results. Figure 5.4 illustrated in a simplified way that we obtain a higher difference between results to higher extinction, suggesting that dust extinction could largely explain this observed difference. It is important to note that this extinction is in the visible band, so its impact will be smaller in the infrared range.

Comparing our results with the relation established by Lilly et al. (2013) for the main sequence at a redshift of 1.17, we find that our results are consistent, considering the large scatter of the data. According to the literature, the location of galaxies within this relation implies that they are actively star-forming galaxies, indicating that our six galaxies are star-forming. This is consistent with [OII] emission in all galaxies.

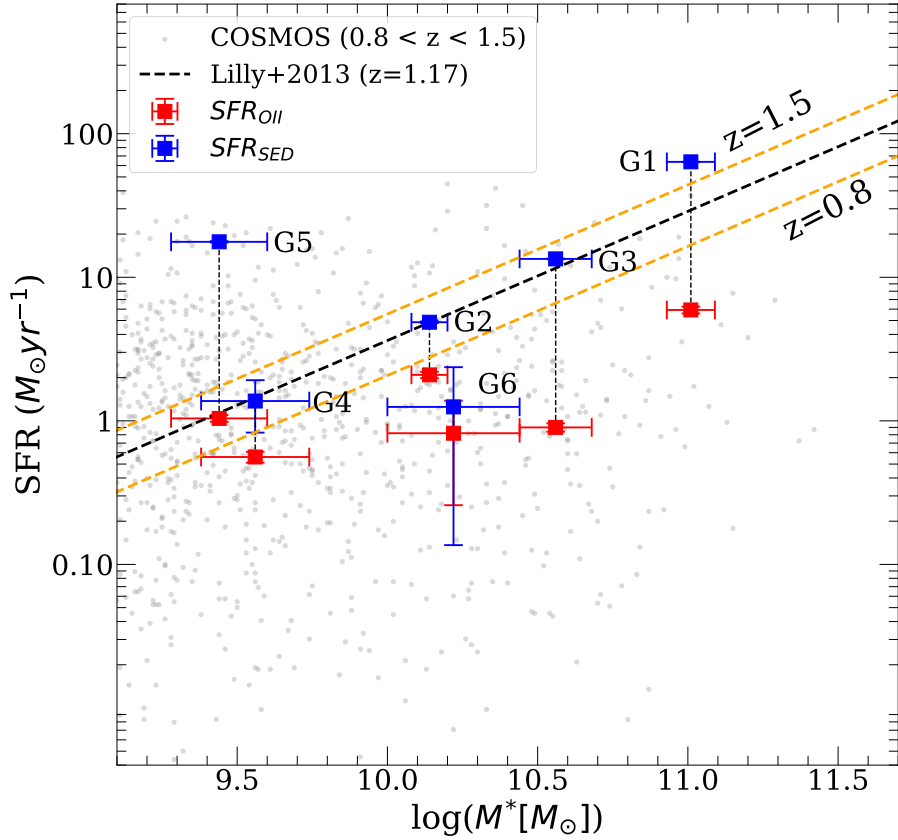


Figure 5.3 Stellar masses versus SFR for the six galaxies, in red those measured according to [OII] and in blue those obtained according to the SED fit. For reference, the gray dots selected by mass between $0.8 < z < 1.5$ in the COSMOS field of CANDELS/3D-HST (Skelton et al., 2014). The SFRs were calculated with a SED fit for COSMOS, assuming a stellar population synthesis of Bruzual & Charlot (2003) with an IMF and solar metallicity of Chabrier (2003). They are also corrected for galactic extinction. The dashed black line and orange lines show the main sequence star-formation rate of Lilly et al. (2013) at $z=1.17$ and; $z=0.8$ and $z=1.5$.

5.2 Absorption-Line analysis: MgII

We used the MUSE spectra for the analysis of the MgII absorption lines. Figure 5.5 shows the absorptions for the arc and contour images at $z = 1.167$.

One of our research goals is to understand which galaxies of the group are responsi-

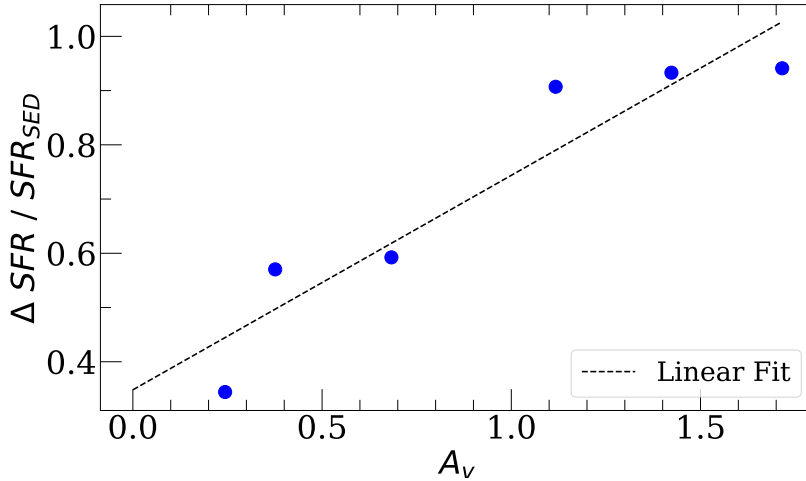


Figure 5.4 The blue dots represent the dust extinction (A_V) of each galaxy as a function of the normalized difference between the values calculated for the SFR according to [OII] and SED fitting. The black dashed line shows the linear fit described by the equation $0.4A_V+0.35$.

ble for the presence of the absorption in the arc. The shape of the absorption lines in the spectra suggests the possibility that no single galaxy is responsible for the absorption, unlike what has been observed in previous studies for another field (Tejos et al., 2021). In the case of the arc, the first absorption line shows a double minimum, leading us to believe that the absorption is caused by more than one contribution (see Appendix F for more details on the Gaussian fit). Furthermore, comparing the line widths in Tejos et al. (2021) and our results, we see that our lines are broader, which may also imply multiple contributions compared to G1 in SGASJ1226.

We conducted an initial analysis and plotted the expected locations of the MgII lines for the four nearest galaxies. All four lines matched the observed absorption, which blended with the Arc, Arc-1, and Arc-2 absorption. This suggests that multiple galaxies may be responsible for the observed absorption.

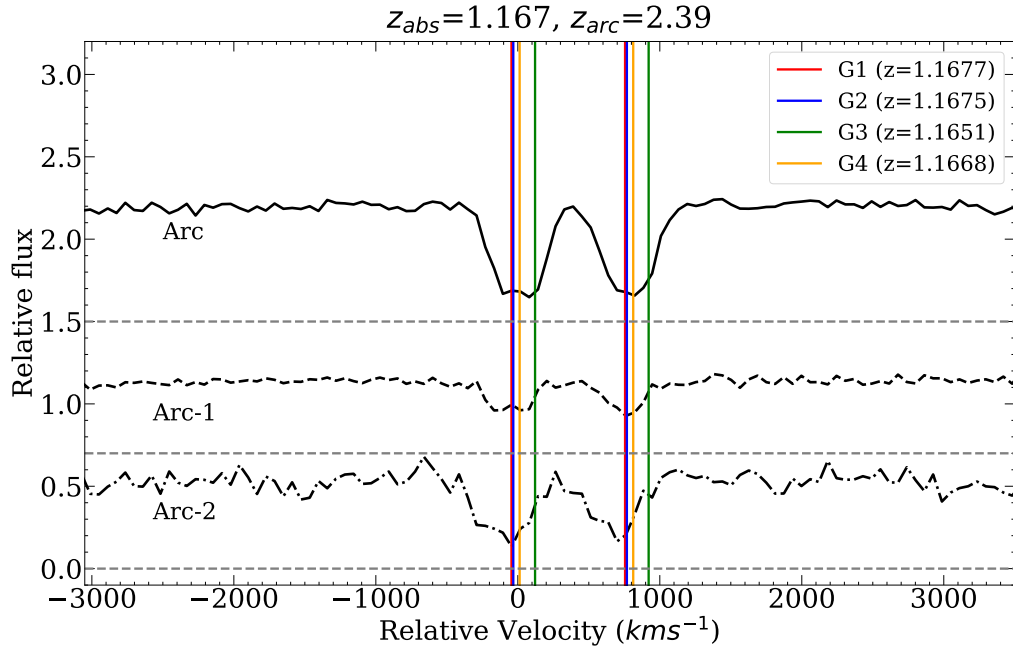


Figure 5.5 MgII absorption for the Arc and contour images 1 (Arc-1) and 2 (Arc-2). The flux is normalized to the maximum of each spectra. Each spectra has a factor added for plot display. In gray dashed line is the zero level of each. Continuous lines are shown where there may be absorption from each galaxy in the group at different redshifts. Only the closest G's are shown.

5.2.1 Equivalent width

We estimated the local continuum for the spectra by fitting a straight line to featureless regions on either side of the expected MgII wavelengths. Then we normalized the spectra to make the fit. We measured the equivalent width (EW) in the spectra in the rest frame by fitting double inverted Gaussian profiles. The EW was calculated as follows:

$$EW_0(1+z) = EW = \sqrt{2\pi}|A|\sigma \quad (5.2)$$

Where $|A|$ represents the amplitude of the Gaussian and σ the standard deviation. The results are shown in Table 5.3. In what follows, we worked with the equivalent width given by the first line of the MgII doublet. The errors in the flux measurement were estimated from the amplitude, and standard deviation of the Gaussian fit as an

Table 5.3. Equivalent Width and Impact Parameter

Object	$W_r(\text{\AA})$	D(kpc)
Arc	3.20 ± 0.05	16.86
Arc-1	1.48 ± 0.08	26.33
Arc-2	2.53 ± 0.19	18.15

Note: The impact parameters were calculated in relation by their closest galaxy as: G2, G3 and G4, in the order of Arc, Arc-1 and Arc-2.

error propagation. Once more we do not consider systematic errors.

The arc exhibits the largest equivalent width $\approx 3.2 \text{ \AA}$, followed by Arc-2 and Arc-1. Because the CGM of galaxies absorbs the MgII, if there are multiple galaxies in the lines of sight to the background source, each can contribute to the absorption observed in the spectra.

Furthermore, galaxy interactions can modify the distribution and dynamics of gas in the CGM. These changes could influence the amount and distribution of MgII absorption in the spectra. In the case of non-interacting galaxies, we could assume individual contributions to the absorption. We take a simplified approach and consider that each galaxy contributes individually to the absorption rather than considering them as a group.

Absorption is also related to the distance at which the galaxies in the group are located according to Nielsen et al. (2013). To address this aspect, we decided to calculate the impact parameters, which will give us information about the distances of the objects in the plane where the absorption takes place.

5.2.2 Impact parameter

First, the positions of all the objects studied were delensed by the lensing equation, using deflection matrix predicted by a lensing model (Fischer et al., 2019). The impact

parameters were calculated in the absorption plane $z=1.167$ and from the centroids of the objects. We will first calculate all impact parameters to the arc and its contour images, assuming that the absorption is produced only by their closest galaxy. The results are in Table 5.3.

Figure 5.6 shows the impact parameters versus equivalent width for Arc, Arc-1 and Arc-2. In addition, we see the relation given by Nielsen et al. (2013) in conjunction with the range of 1, 2, and 3 σ of the relation. The absorption of the galaxies studied by Nielsen et al. (2013) was also detected by the MegaSaura survey in the same way as our field.

Our data are above the established relation between 2 to 3 σ . Therefore, the total contribution is not fully explained by considering only one of the galaxies as responsible for the absorption.

To verify the initial hypothesis that the absorption is not produced by only one of the galaxies, we performed estimates of the equivalent widths using the relation proposed by Nielsen et al. (2013), based on the impact parameters measured from the galaxies to the objects (Arc, Arc-1 and Arc-2). We then compute a scaling factor that allows the sum of the predicted equivalent widths to fit the total EW value measured in the spectrum. This factor is determined as $f = EW_{total}/EW_{sum}$, where EW_{total} represents the total measured value and EW_{sum} is the sum of the values predicted by the theory. By applying this scaling factor, we observe that for Arc and Arc-2, the results are considerably close to the expected relation, with approximate values of $f_{ARC} \sim 1.2$ and $f_{ARC-2} \sim 1.1$. This leads us to conclude that the assumption of individual contributions from each galaxy can explain what happens in the field.

Furthermore, we reiterate that the main galaxies in this analysis are G1, G2, G3, G4 and partly G5 since G6 has outlying impact parameters that result in a minimal total EW contribution compared to the others. As for Arc-1, we obtain $f_{ARC-1} \sim 0.7$, and the relation remains within 1σ , indicating that the results are similarly consistent. This difference could be because we consider a linear sum of the estimated equivalent widths.

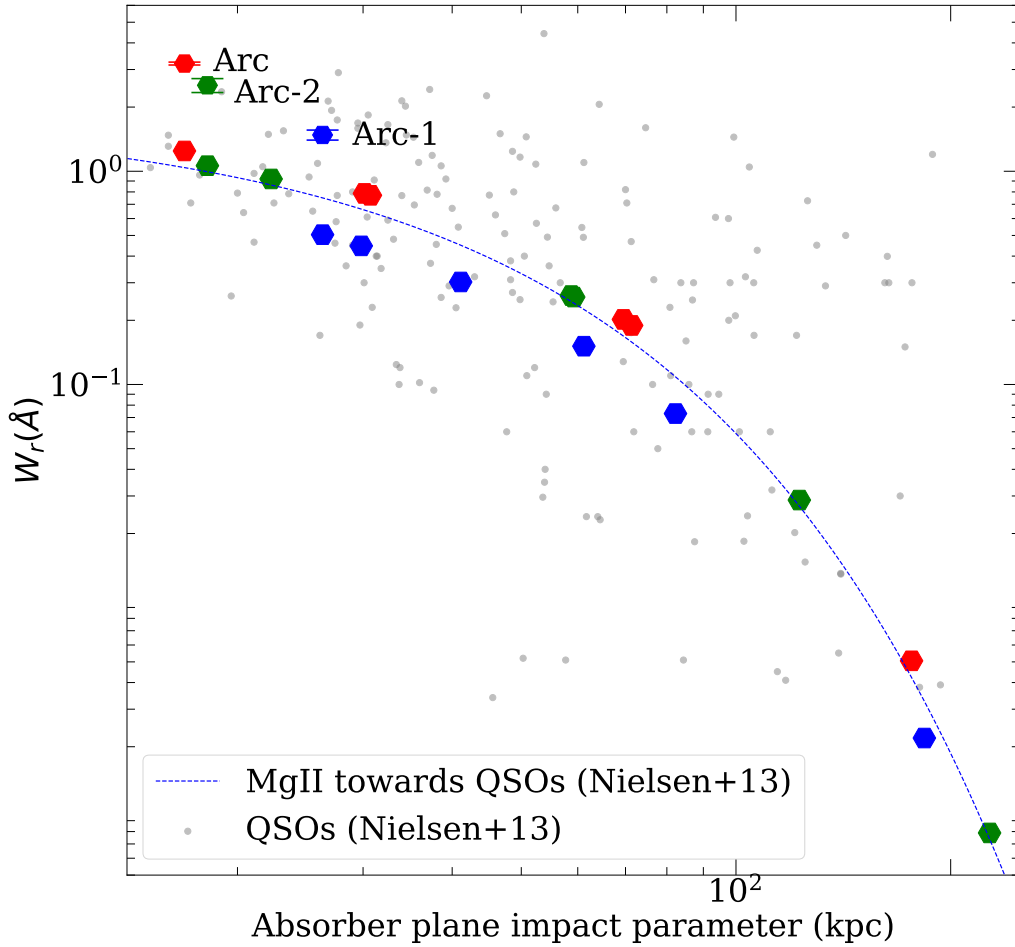


Figure 5.6 The figure compares the calculated equivalent widths as a function of the impact parameter. At the top, the results for Arc, Arc-1 and Arc-2 are shown. Their calculated impact parameters are those measured *by their closest galaxy* in the absorber plane. The blue dashed line represents the relation proposed by Nielsen et al. (2013). The blue sectors represent 1, 2 and 3 σ of the relation, varying their transparency accordingly. The other dots correspond to the equivalent width estimates according to Nielsen et al. (2013) using the impact parameter measured from each of the six galaxies to each object. Red dots indicate predictions for Arc, blue dots for Arc-1 and green dots for Arc-2. A scaling factor allows the sum of the dots to result in the total measured equivalent width.

Since we know that absorption is highly dependent on the mass of the galaxies, a more thorough analysis of the precise contribution of each galaxy to the absorption should

be carried out by assigning weights to each galaxy according to its total calculated mass.

5.3 Kinematics

5.3.1 Velocity to [OII] and MgII: z=1.167

We obtained the velocities from the shift provided by the Gaussian fitting of the [OII] and MgII reference lines. For the "G" galaxies, we see the velocities to [OII] and the arc and its contour images to MgII.

Figure 5.7 shows, as a complete visualization, the galaxies colored by their velocities and their delensed positions. In addition, circles with their radius are shown in blue as the obtained virial radius.

Considering the virial radius as the boundary of the CGM, we can identify which galaxies in the group are related to the arc and contour images. The Arc lies within the circles associated with G1, G2, and G3. Arc-1 is found in G1, G2, G3 and partially in G4. Finally, Arc-2 is found in G1, G2, G3 and G4. In addition, how large the circle gives us an indication of the masses of the galaxies that contribute to the observed absorption in the arc.

We consider positive velocities as the galaxies move away from the observer and negative velocities as they approach. We note that galaxies G1, G2 and G5 are moving away, while G3 and G4 are moving closer. We do not consider G6 as part of this system. As for Arc, Arc-1 and Arc-2, we note that while Arc is moving away, Arc-2 is moving closer. This gives us a first insight into the kinematics of the gas in the absorption plane.

Based on this, the velocities suggest the existence of non-aleatory motion in the system. Figure 5.8 shows, a horizontal representation of the movements of the galaxies and the gas (arc) is presented. It is observed that the fit performed for both sets of points maintains the same direction, suggesting the presence of a rotation in the same

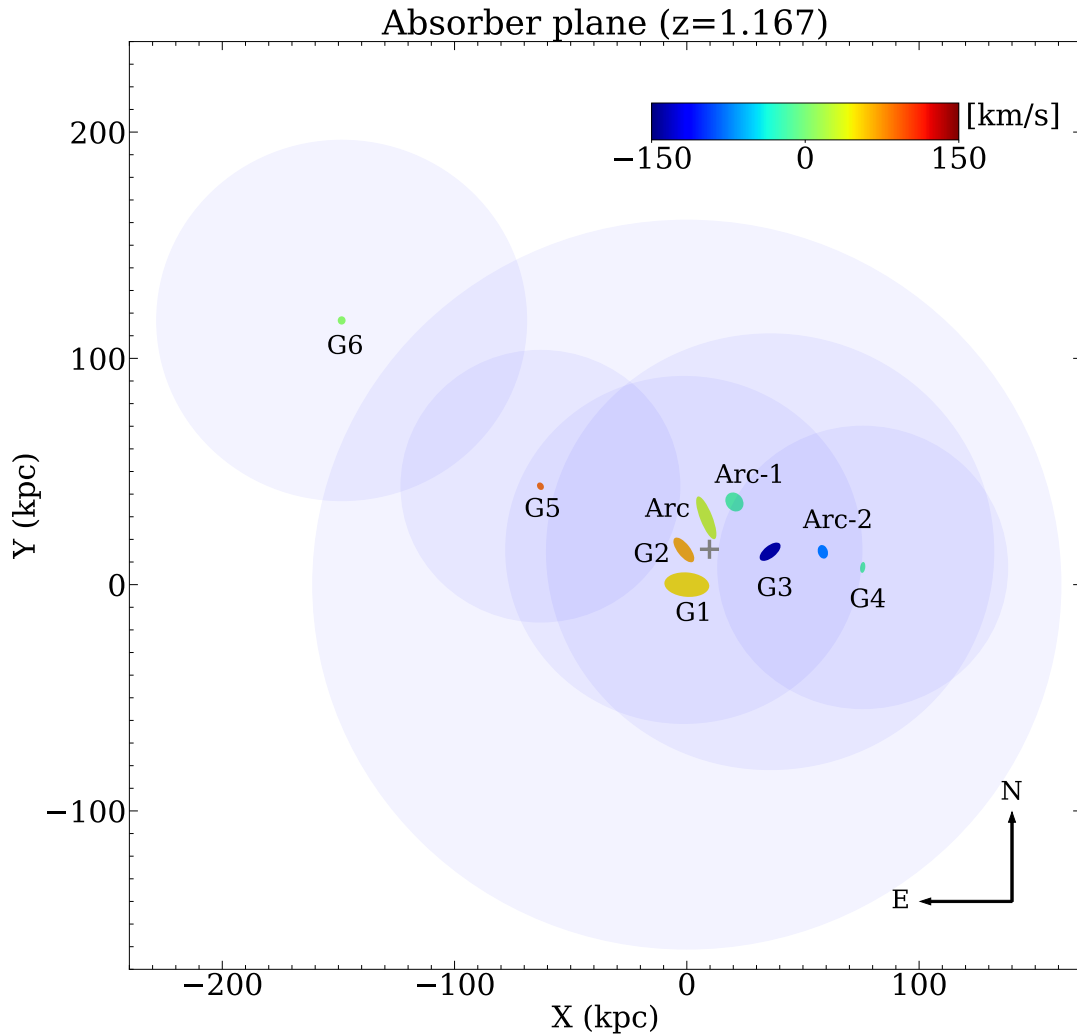


Figure 5.7 Galaxies with their delensed positions in the absorption plane at $z=1.167$. We show their morphology from the apertures in the photometric and spectroscopic calculations. Their velocities are colored according to the colorbar located in the upper right corner. The zero velocity is defined as the average velocity of the system. The blue circles represent the virial radius of the galaxies, centered on their position. In a grey cross, the center of mass of the five galaxies system.

direction for both galaxy stars and CGM gas. In addition, the center of mass on the X-axis and the mass-weighted velocity of the five main galaxies are calculated. It is observed that the intersection coincides with the derived relation for the galaxies, which

leads us to assume that the rotation axis of the stars is at the center of mass.

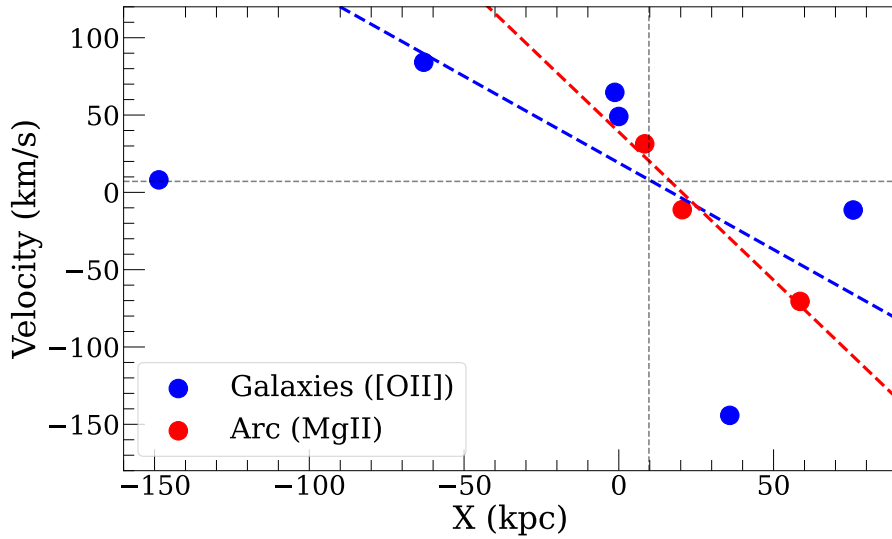


Figure 5.8 Figure 5.7 shows, a horizontal view of the X axis (kpc) representing galaxy positions, arc and contour images versus object velocities is shown. The blue dots correspond to the galaxies, while the red dots represent the arc-related objects. Linear fits were performed on each data set, shown as dashed lines with the corresponding color. The fit for the blue points is $-1.12x+19.05$, while the fit for the red points is $-1.92x+39.07$. In addition, the center of mass and mass-weighted velocity are shown by gray dashed lines.

Chapter 6

Conclusion and future work

Multiband HST data and the MUSE data cube were used for photometry and spectroscopy of the SGASJ0033 field. Our target was the main galaxies of a group that are at an intermediate redshift of $z=1.167$ and produce the absorption seen in the field arc at the same redshift. In addition, [OII] emission is observed in the galaxies. The cluster producing the arc due to a gravitational lensing effect is at $z_{CL}=0.4716$, and the bright lensed galaxy at $z_{ARC}=2.39$.

Photometry was obtained in four bands: F555W, F814W, F105W and F140W, and corrected for magnification and galactic extinction. For spectroscopy, spectra were obtained within the MUSE data cube without the central star. The star was modeled using a 2D Moffat. The spectra were also corrected for magnification and galactic extinction.

Galaxies were analyzed for stellar mass, dark matter halo mass, virial radius, maximum circular velocity, and star formation rate given by SED fitting and [OII] emission. In addition, using the technique of arc-tomography in bright point sources, we used the potential of multiple arc imaging to study the MgII absorptions produced by the CGM at $z=1.167$. We measured equivalent widths in the absorption and calculated impact parameters to achieve this. Finally, a kinematic study of the field to [OII] emission in galaxies and MgII in the arc was initiated.

Our main results in this work can be summarized as follows:

- We obtained results on the properties of the group’s galaxies that were consistent with previous studies. We also compared the stellar mass of G1 with a study by Solimano et al. (2021) and found a difference of 0.46 dex, which can be attributed to differences in the methods used to calculate the stellar mass values.
- When calculating the SFR using SED fitting and [OII], some results show noticeable differences. By examining the dust extinction of each galaxy, we have discovered a correlation between the normalized difference and the amount of A_V (Figure 5.4). Based on this, the observed differences may be because $SFR_{[OII]}$ was not corrected for A_V .
- By examining the M_* versus SFR relation (Figure 5.3), we have determined that our data are consistent with the relation established by Lilly et al. (2013) for the SFR main sequence. Although our data has a considerable scatter, we can conclude that our group’s galaxies are star-forming, as evidenced by the observed [OII] emission.
- The MgII absorptions suggest that the absorption is not produced from a CGM halo of a single galaxy. Through the use of plotted data (see Figure F.1) and an analysis of impact parameters (see Figure 5.6), the absorption may be produced by more than one galaxy. We considered individual contributions without considering an absorption that the group could give.
- We examined the galaxies nearest to the arc and the contour images in the absorption plane using Figure 5.7. We further concluded from their velocities that the stars in the galaxies appear to show non-aleatory motion and rotation with respect to the center of mass. The gas seems to rotate in the same direction (Figure 5.8).

These results do not demonstrate that each halo is related to the particular galaxies since there may be only one halo for the whole group. This would indicate that the rotation may be related to interactions within the group and thus could affect the CGM.

In addition, it is important to mention that many of the reported uncertainties were underestimated, considering that systematic errors highly influence them.

For future work, it is expected to follow the final kinematic analysis using velocity maps to get a clearer idea of the field behavior. In addition, this will allow us to compare results in emission and absorption on the CGM.

Bibliography

ARCTOMO 2023, Arctomo - publications and theses, <https://sites.google.com/view/arctomo/publications-and-theses>

Bacon R., et al., 2023, , 670, A4

Blumenthal G. R., Faber S. M., Primack J. R., Rees M. J., 1984, , 311, 517

Bouché N., Murphy M. T., Péroux C., Csabai I., Wild V., 2006, Monthly Notices of the Royal Astronomical Society, 371, 495

Bruzual G., Charlot S., 2003, , 344, 1000

Cardelli J. A., Clayton G. C., Mathis J. S., 1989, , 345, 245

Carnall A. C., McLure R. J., Dunlop J. S., Davé R., 2018, Monthly Notices of the Royal Astronomical Society, 480, 4379

Casertano S., et al., 2000, The Astronomical Journal, 120, 2747

Chabrier G., 2003, Publications of the Astronomical Society of the Pacific, 115, 763

Chen H.-W., Helsby J. E., Gauthier J.-R., Shectman S. A., Thompson I. B., Tinker J. L., 2010, The Astrophysical Journal, 714, 1521

Dutta R., et al., 2020, Monthly Notices of the Royal Astronomical Society, 499, 5022

Faber S. M., et al., 2007, , 665, 265

Faucher-Giguere C.-A., Oh S. P., 2023, Key Physical Processes in the Circumgalactic Medium ([arXiv:2301.10253](https://arxiv.org/abs/2301.10253))

- Fischer T. C., et al., 2019, The Astrophysical Journal, 875, 102
- Fruchter A. S., Hook R. N., 2002, Publications of the Astronomical Society of the Pacific, 114, 144
- Gaia Collaboration et al., 2018, , 616, A1
- Gal R., 2023, Roy Gal's Notes on SExtractor, https://home.ifa.hawaii.edu/users/rgal/science/sextor_notes.html#:~:text=SExtractor
- Gao Y., et al., 2018, The Astrophysical Journal, 869, 15
- Ginsburg A., Sokolov V., de Val-Borro M., Rosolowsky E., Pineda J. E., Sipőcz B. M., Henshaw J. D., 2022, The Astronomical Journal, 163, 291
- Hogg D. W., et al., 1998, The Astronomical Journal, 115, 1418
- Holwerda B. W., 2017, Aperture photometry, <https://sextractor.readthedocs.io/en/latest/Photom.html>
- Hubble E. P., 1926, , 64, 321
- Kashino D., et al., 2022, The Astrophysical Journal, 925, 82
- Kennicutt Robert C. J., 1992, , 388, 310
- Kereš D., Katz N., Fardal M., Davé R., Weinberg D. H., 2009, Monthly Notices of the Royal Astronomical Society, 395, 160
- Kroupa P., Boily C. M., 2002, , 336, 1188
- Labbé I., et al., 2023, Nature, 616, 266
- Lilly S. J., Carollo C. M., Pipino A., Renzini A., Peng Y., 2013, The Astrophysical Journal, 772, 119
- Lopez S., et al., 2018, , 554, 493
- Lopez S., et al., 2020, , 491, 4442

- MPDAF 2023, Moffat Model 2, <https://mpdaf.readthedocs.io/en/latest/api/mpdaf.MUSE.MoffatModel2.html>
- Madau P., Dickinson M., 2014, , 52, 415
- McKee C. F., Ostriker E. C., 2007, Annual Review of Astronomy and Astrophysics, 45, 565
- Ménard B., Fukugita M., 2012, The Astrophysical Journal, 754, 116
- Mo H. J., Mao S., White S. D. M., 1998, Monthly Notices of the Royal Astronomical Society, 295, 319
- Moffat A. F. J., 1969, , 3, 455
- Moster B. P., Somerville R. S., Maulbetsch C., van den Bosch F. C., Macciò A. V., Naab T., Oser L., 2010, The Astrophysical Journal, 710, 903
- Muratov A. L., Kereš D., Faucher-Giguère C.-A., Hopkins P. F., Quataert E., Murray N., 2015, Monthly Notices of the Royal Astronomical Society, 454, 2691
- Nielsen N. M., Churchill C. W., Kacprzak G. G., 2013, The Astrophysical Journal, 776, 115
- Peebles P. J. E., 1982, , 263, L1
- Péroux C., Howk J. C., 2020, Annual Review of Astronomy and Astrophysics, 58, 363
- Pessa I., Tejos N., Moya C., 2018, PyMUSE: a Python package for VLT/MUSE data ([arXiv:1803.05005](https://arxiv.org/abs/1803.05005))
- Rigby J. R., et al., 2018a, VizieR Online Data Catalog, p. J/AJ/155/104
- Rigby J. R., et al., 2018b, VizieR Online Data Catalog, p. J/ApJ/853/87
- Salim S., Lee J. C., Davé R., Dickinson M., 2015, The Astrophysical Journal, 808, 25
- Schawinski K., et al., 2014, Monthly Notices of the Royal Astronomical Society, 440, 889

- Schlafly E. F., Finkbeiner D. P., 2011, The Astrophysical Journal, 737, 103
- Schultz G. V., Wiemer W., 1975, , 43, 133
- Skelton R. E., et al., 2014, , 214, 24
- Solimano M., et al., 2021, Astronomy & Astrophysics, 655, A42
- Tejos N., et al., 2021, Monthly Notices of the Royal Astronomical Society, 507, 663
- Tumlinson J., Peeples M. S., Werk J. K., 2017, Annual Review of Astronomy and Astrophysics, 55, 389
- Weilbacher P. M., et al., 2020, , 641, A28
- Werk J. K., et al., 2014, The Astrophysical Journal, 792, 8
- Wuyts E., et al., 2014, The Astrophysical Journal, 789, L40

Appendix A

MUSE: White-Light Image

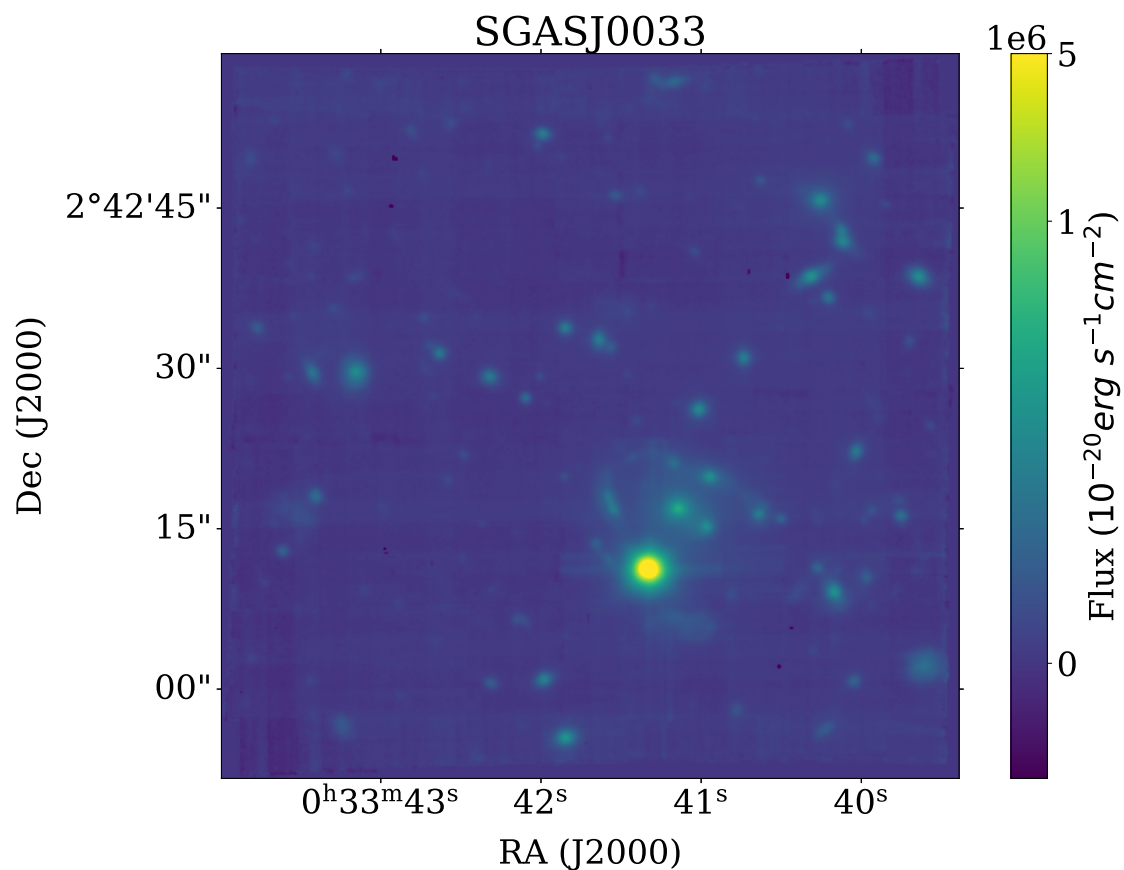


Figure A.1 White light image of MUSE data cube collapsed in all wavelengths of the spectral range. It is normalized to a logarithmic scale.

Appendix B

Photutils apertures

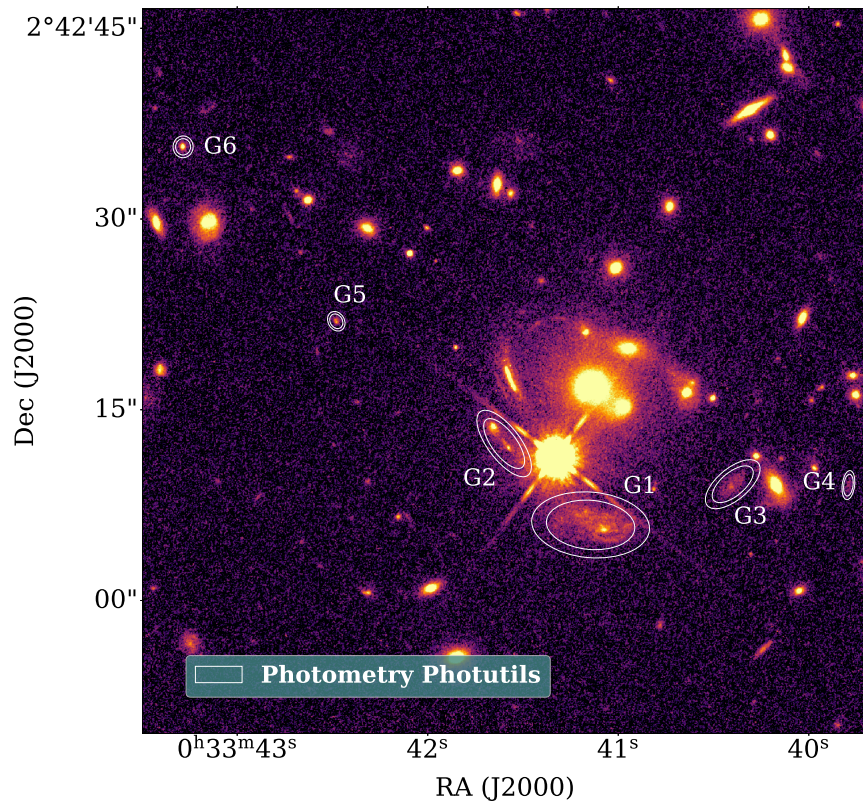


Figure B.1 Elliptical apertures for G1, G2, G3, G4, G5 and G6 for the photometry measurement and annular apertures for the background estimation for each source.

Appendix C

Star modelling

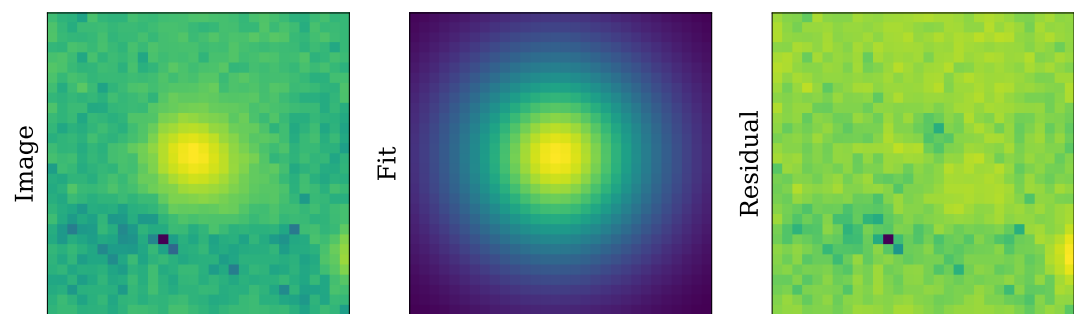


Figure C.1 Image, fit and residuals for the third star in the field. Images are normalized to logarithmic scale.

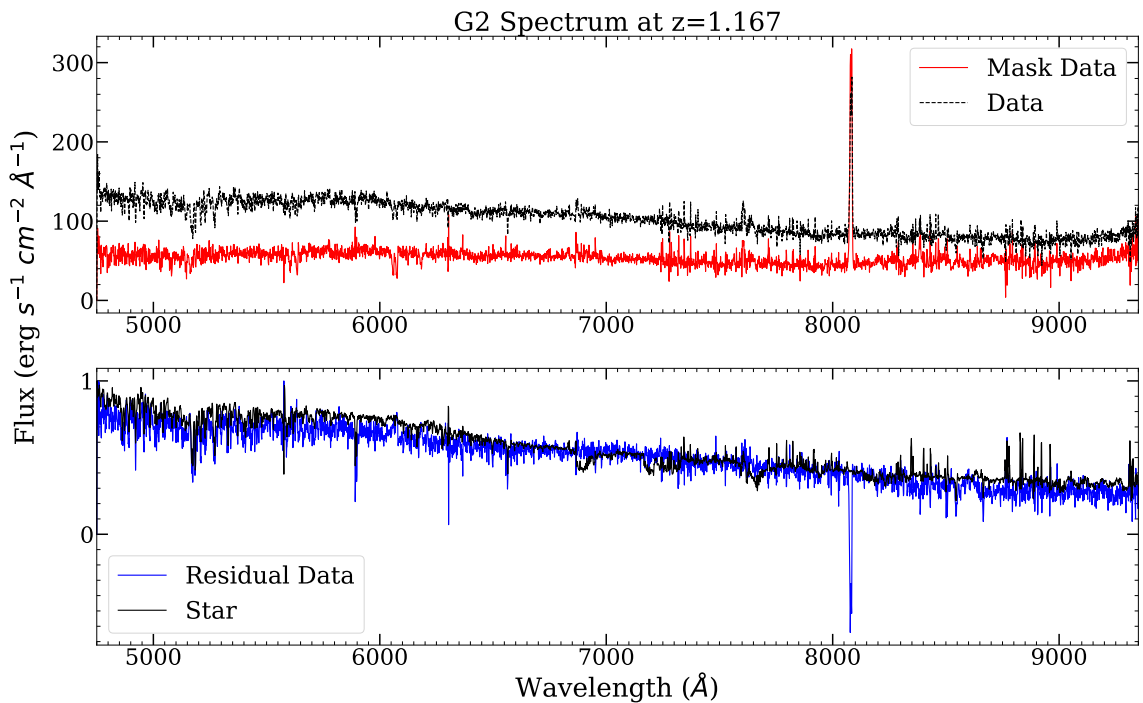


Figure C.2 At the top, the spectra obtained with PyMUSE in the original cube (Data) and the cube without the star (Mask Data) for G2. The wavelength range is at $z=1.167$. At the bottom are the star and recovered spectra given by subtracting the spectra at the top.

Appendix D

BAGPIPES fitting

The parameters and priors given to BAGPIPES are given below.

```
1 dblplaw = {}
2 dblplaw["tau"] = (0., 15.)
3 dblplaw["alpha"] = (0.01, 1000.)
4 dblplaw["beta"] = (0.01, 1000.)
5 dblplaw["alpha_prior"] = "log_10"
6 dblplaw["beta_prior"] = "log_10"
7 dblplaw["massformed"] = (1., 15.)
8 dblplaw["metallicity"] = (0.1, 2.)
9 dblplaw["metallicity_prior"] = "log_10"

10
11 nebular = {}
12 nebular["logU"] = -3.

13
14 dust = {}
15 dust["type"] = "CF00"
16 dust["eta"] = 2.
17 dust["Av"] = (0., 2.0)
18 dust["n"] = (0.3, 2.5)
```

```

19 dust["n_prior"] = "Gaussian"
20 dust["n_prior_mu"] = 0.7
21 dust["n_prior_sigma"] = 0.3
22
23 fit_instructions = {}
24 fit_instructions["redshift"] = 1.167
25 fit_instructions["t_bc"] = 0.01
26 fit_instructions["dblplaw"] = dblplaw
27 fit_instructions["nebular"] = nebular
28 fit_instructions["dust"] = dust
29
30 fit_instructions["veldisp"] = (1., 1000.) #km/s
31 fit_instructions["veldisp_prior"] = "log_10"
32
33 calib = {}
34 calib["type"] = "polynomial_bayesian"
35
36 calib["0"] = (0.5, 1.5) # Zero order is centred on 1,
                           at which point there is no change to the spectrum.
37 calib["0_prior"] = "Gaussian"
38 calib["0_prior_mu"] = 1.0
39 calib["0_prior_sigma"] = 0.25
40
41 calib["1"] = (-0.5, 0.5) # Subsequent orders are
                           centred on zero.
42 calib["1_prior"] = "Gaussian"
43 calib["1_prior_mu"] = 0.
44 calib["1_prior_sigma"] = 0.25
45
46 calib["2"] = (-0.5, 0.5)
47 calib["2_prior"] = "Gaussian"

```

```

48 calib["2_prior_mu"] = 0.
49 calib["2_prior_sigma"] = 0.25
50
51 fit_instructions["calib"] = calib
52
53 mlpoly = {}
54 mlpoly["type"] = "polynomial_max_like"
55 mlpoly["order"] = 2
56
57 noise = {}
58 noise["type"] = "white_scaled"
59 noise["scaling"] = (1., 10.)
60 noise["scaling_prior"] = "log_10"
61 fit_instructions["noise"] = noise

```

The fitting achieved for the rest of the galaxies is shown below:

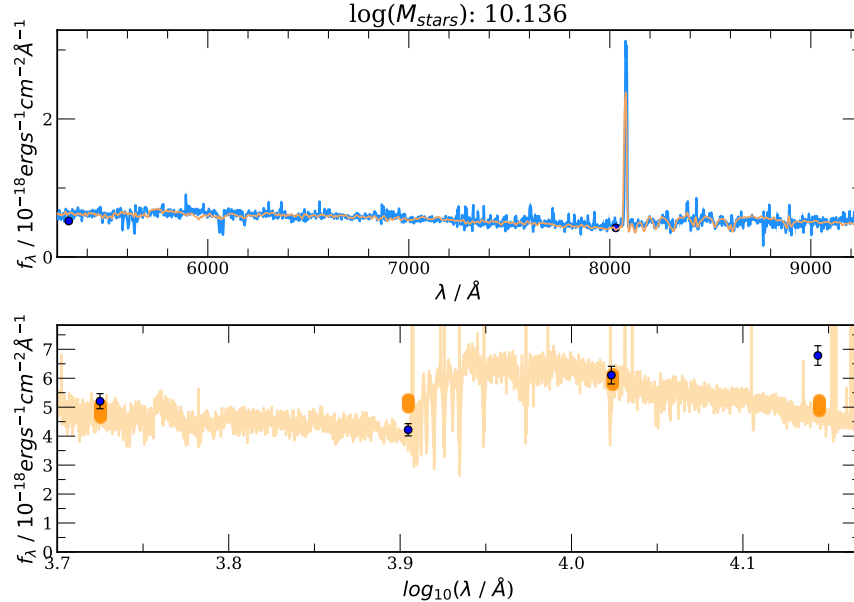


Figure D.1 For G2, the fit made by BAGPIPES in orange for the HST photometry and the MUSE spectrum.

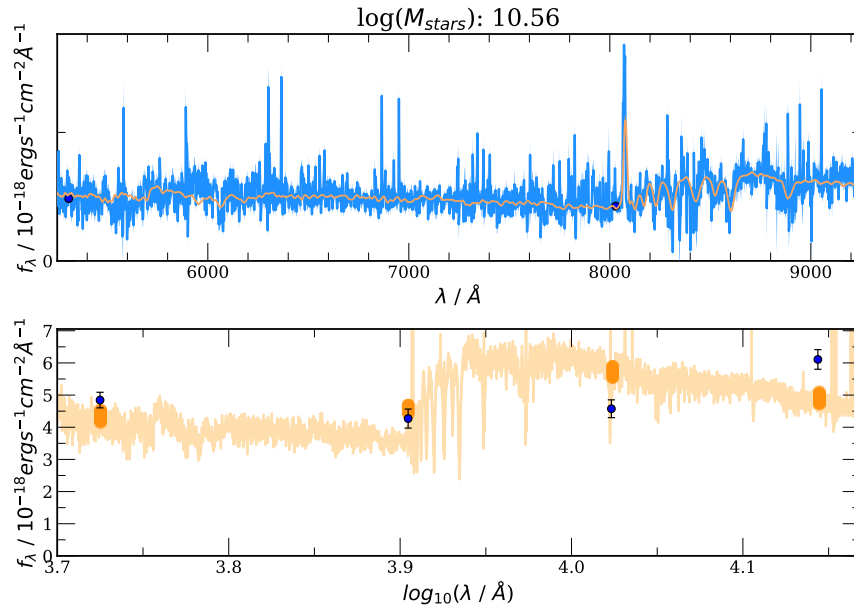


Figure D.2 For G3, the fit made by BAGPIPES in orange for the HST photometry and the MUSE spectrum.

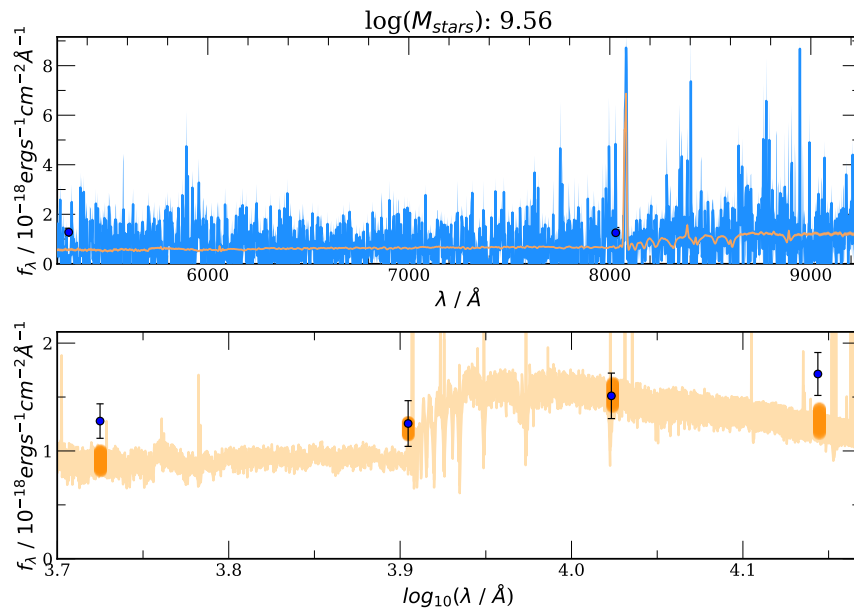


Figure D.3 For G4, the fit made by BAGPIPES in orange for the HST photometry and the MUSE spectrum.

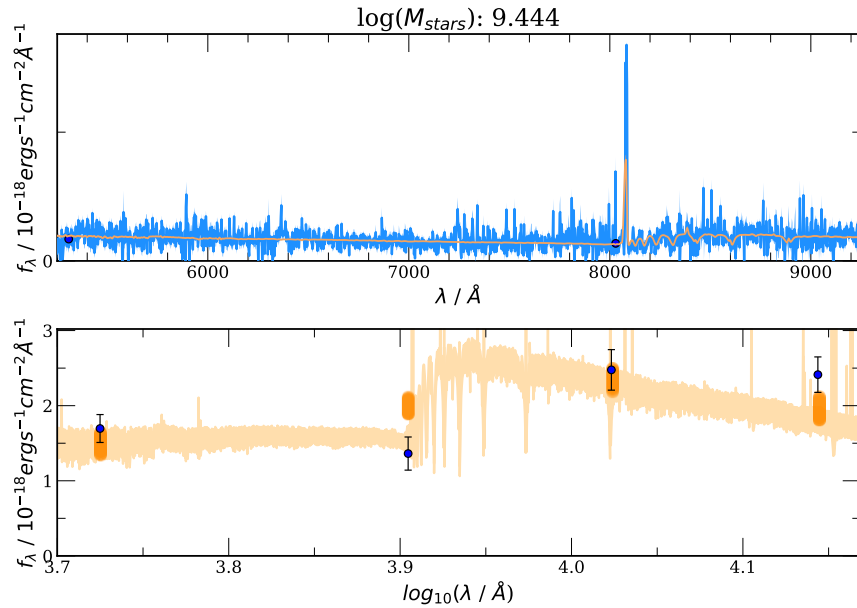


Figure D.4 For G5, the fit made by BAGPIPES in orange for the HST photometry and the MUSE spectrum.

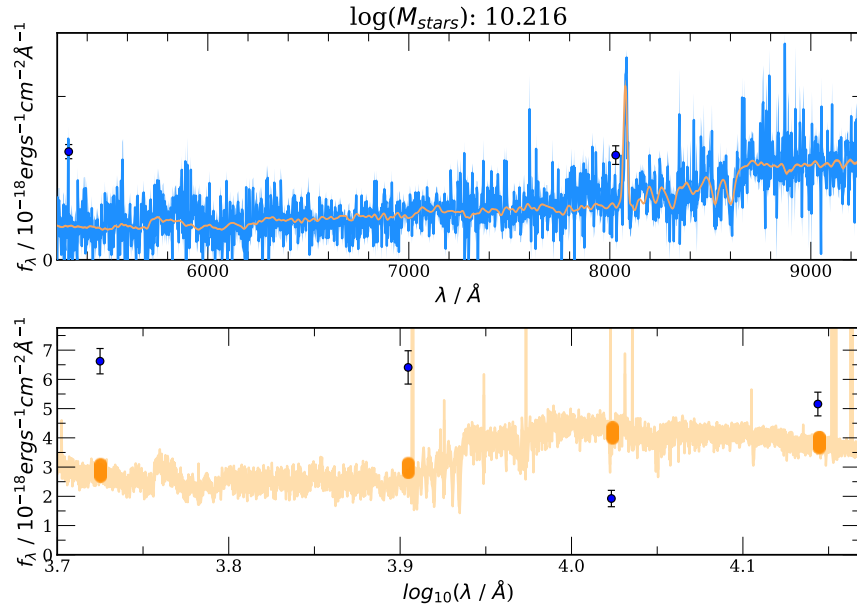


Figure D.5 For G6, the fit made by BAGPIPES in orange for the HST photometry and the MUSE spectrum.

Appendix E

Halo-mass estimation

Approximate results are shown in Figure E.1 according to the relation given by Moster et al. (2010) (equation E.1).

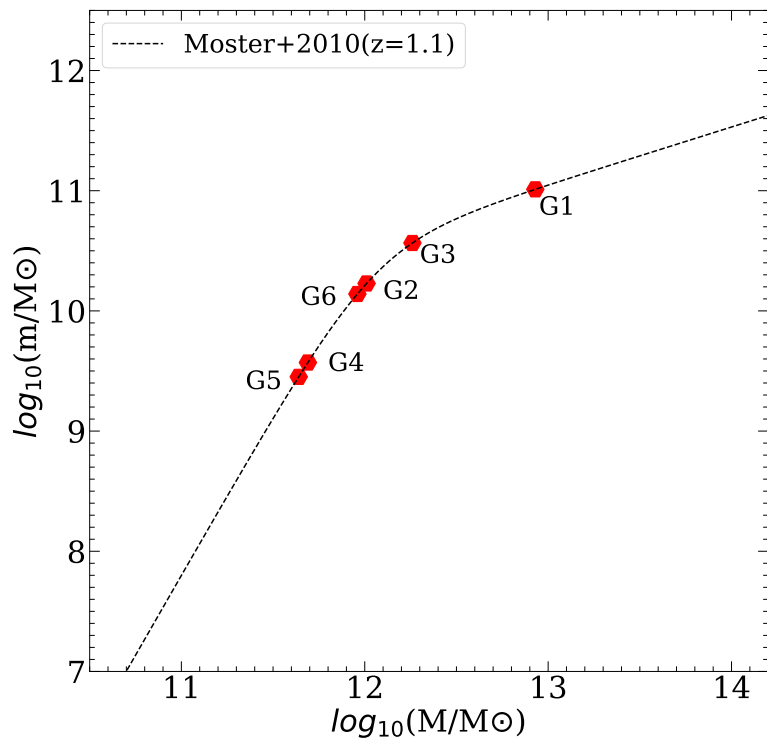


Figure E.1 In red, the values found for M are given by the relation for the six galaxies.

Table E.1. Table 6: Moster et al. (2010).

z	$\log(M_1)$	$(m/M)_0$	β	γ
1.1	12.05 ± 0.18	0.0175 ± 0.0060	$1.66_{-0.26}^{+0.31}$	0.52 ± 0.40

$$m_s(M) = 2M \left(\frac{m_s}{M}\right)_0 \left[\left(\frac{M}{M_{1s}}\right)^{-\beta_s} + \left(\frac{M}{M_{1s}}\right)^{\gamma_s} \right]^{-1} \quad (\text{E.1})$$

Where m_s is the stellar mass, M is the dark matter halo mass, and $\left(\frac{m_s}{M}\right)_0$, M_{1s} , β_s and γ_s parameters. The calculated values for $z=1.1$ given in Table E.1 were used for these.

Appendix F

MgII absorption estimation

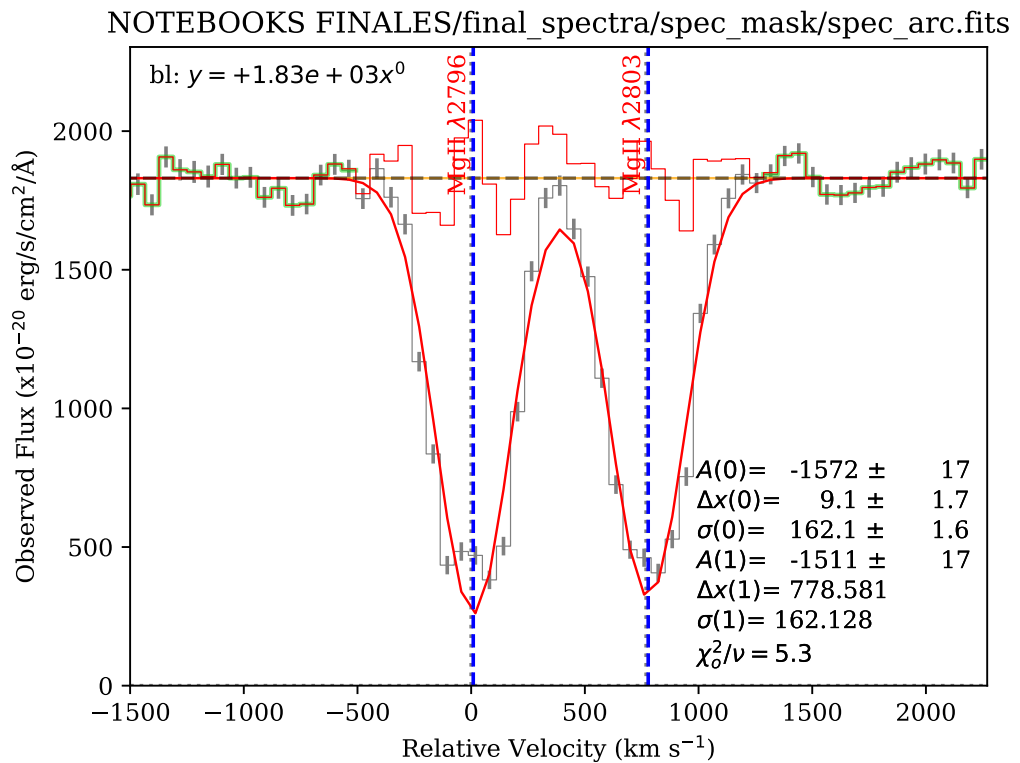


Figure F.1 Fitting made with `pyspeckit` an inverted double Gaussian for the absorption of MgII in the arc. In green, the continuum. In red, the fit and blue, the wavelength-recognized lines. Code from C. Ledoux.